

CORRECTING THE  $z \sim 8$  GALAXY LUMINOSITY FUNCTION FOR GRAVITATIONAL LENSING  
MAGNIFICATION BIASCHARLOTTE A. MASON<sup>1</sup>, TOMMASO TREU<sup>1,2</sup>, KASPER B. SCHMIDT<sup>1</sup>, THOMAS E. COLLETT<sup>3,4</sup>, MICHELE TRENTI<sup>5,7</sup>, PHILIP J. MARSHALL<sup>6</sup>, ROBERT BARONE-NUGENT<sup>7</sup>, LARRY D. BRADLEY<sup>8</sup>, MASSIMO STIAVELLI<sup>8</sup>, AND STUART WYITHE<sup>7</sup><sup>1</sup> Department of Physics, University of California, Santa Barbara, CA, 93106-9530, USA<sup>2</sup> Department of Physics and Astronomy, UCLA, Los Angeles, CA, 90095-1547, USA<sup>3</sup> Institute of Astronomy, University of Cambridge, Madingley Rd, Cambridge, CB3 0HA, UK<sup>4</sup> Institute for Cosmology and Gravitation, University of Portsmouth, Burnaby Road, Portsmouth, PO1 3FX, UK<sup>5</sup> Kavli Institute for Cosmology and Institute of Astronomy, University of Cambridge, Madingley Road, Cambridge, CB3 0HA, UK<sup>6</sup> Kavli Institute for Particle Astrophysics and Cosmology, Stanford University, 452 Lomita Mall, Stanford, CA 94035, USA<sup>7</sup> School of Physics, University of Melbourne, Parkville, Victoria, Australia and<sup>8</sup> Space Telescope Science Institute, 3700 San Martin Drive, Baltimore, MD, 21218, USA*Submitted to the Astrophysical Journal, 2015 January 25*

## ABSTRACT

We present a Bayesian framework to account for the magnification bias from both strong and weak gravitational lensing in estimates of high-redshift galaxy luminosity functions. We illustrate our method by estimating the  $z \sim 8$  UV luminosity function using a sample of 97 Y-band dropouts (Lyman break galaxies) found in the Brightest of Reionizing Galaxies (BoRG) survey and from the literature. We find the luminosity function is well described by a Schechter function with characteristic magnitude of  $M^* = -19.85^{+0.30}_{-0.35}$ , faint-end slope of  $\alpha = -1.72^{+0.30}_{-0.29}$ , and number density of  $\log_{10} \Psi^* [\text{Mpc}^{-3}] = -3.00^{+0.23}_{-0.31}$ . These parameters are consistent within the uncertainties with those inferred from the same sample without accounting for the magnification bias, demonstrating that the effect is small for current surveys at  $z \sim 8$ , and cannot account for the apparent overdensity of bright galaxies found recently by Bowler et al. (2014a,b) and Finkelstein et al. (2014). We estimate that the probability of finding a strongly lensed  $z \sim 8$  source in our sample is in the range  $\sim 3 - 15\%$  depending on limiting magnitude. We identify one strongly-lensed candidate and three cases of intermediate lensing in BoRG (estimated magnification  $\mu > 1.4$ ) in addition to the previously known candidate group-scale strong lens. Using a range of theoretical luminosity functions we conclude that that magnification bias will dominate wide field surveys – such as those planned for the Euclid and WFIRST missions – especially at  $z > 10$ . Magnification bias will need to be accounted for in order to derive accurate estimates of high-redshift luminosity functions in these surveys and to distinguish between galaxy formation models.

*Subject headings:* galaxies: high-redshift — galaxies: LF — gravitational lensing: strong

## 1. INTRODUCTION

Accurate measurements of the rest-frame UV luminosity function (LF) are vital for studying the evolution of galaxies at high redshift and reconstructing the physics and timeline of cosmic reionization. In recent years, significant progress has been achieved in measuring the LF out to  $z \sim 8$  and beyond based on images taken with the Hubble Space Telescope in the deep legacy fields and through parallel programs (e.g., Bouwens et al. 2007, 2011; Bradley et al. 2012; Oesch et al. 2012; Robertson et al. 2013; McLure et al. 2013; Schenker et al. 2013; Schmidt et al. 2014a; Bradley et al. 2014; Bouwens et al. 2014; Finkelstein et al. 2014).

From many of these surveys it appears the LF at  $z < 6$  is well fit by a Schechter (1976) function with a power-law slope at faint luminosities and an exponential drop at the bright end, where it is expected that feedback reduces star-formation in the most massive galaxies (Somerville et al. 2012) and dust extinction may reduce the UV flux of galaxies (Cai et al. 2014). The evolution of the LF is expected to be driven by these processes and the evolution of the underlying halo mass function. It is so far unestablished which processes dominate the evolution and

whether there are signification changes in the physical conditions of galaxies forming at high redshifts.

Recent studies by Bowler et al. (2014a,b) and Finkelstein et al. (2014) claimed an over-abundance of galaxies at the bright end of the  $z \geq 6$  LF when compared to the fit of a Schechter (1976) function, although Bouwens et al. (2014) found no evidence for a departure from a Schechter-like form at  $z \sim 4 - 8$ , largely analyzing the same data sets. An over-abundance of bright galaxies may also be apparent in smaller surveys (e.g., Ono et al. 2012; Hathi et al. 2012; Finkelstein et al. 2013). If the departure from an exponential cutoff is confirmed by future observations, this may be an indication of the changing astrophysical conditions of high-redshift galaxies. However, another possible explanation is that the LF remains intrinsically with a Schechter form and the over-abundance of bright galaxies is caused by gravitational lensing magnification bias, which has been predicted to be significant for galaxies at  $z \geq 8$  (Wyithe et al. 2011).

While it has long been recognized that the gravitational lensing effect can be exploited in order to probe intrinsically faint galaxies – in particular behind massive clusters of galaxies at moderate redshift – (e.g., Franx et al. 1997; Ellis et al. 2001; Schmidt et al. 2014b; Atek et al. 2014; Bowler et al. 2014b; Coe et al. 2014; Zitrin

et al. 2014), the effect in blank fields is much less well appreciated.

In fact, gravitational lensing affects all lines of sight, as the trajectory of every photon in the universe is perturbed by the inhomogeneous foreground mass distribution. Though the effect is generally not as strong as in the fields of massive clusters of galaxies, even so-called blank field surveys are affected by gravitational lensing (weak, intermediate, or strong). In practice, owing to the lensing effect, flux-limited surveys include sources that should be below the sample threshold, but have been magnified into the sample. Furthermore, gravitational lensing changes the relation between observed solid angle and cosmic volume with respect to that expected for a perfectly homogeneous universe. At fixed detector field-of-view the intrinsic solid angle observed is smaller for magnification  $\mu > 1$  and vice versa. This phenomenon is called *magnification bias* (e.g., Turner et al. 1984; Wyithe et al. 2001, 2011) and it can change the shape of the observed LF. Thus, it needs to be accounted for in order to derive accurate intrinsic LFs from flux-limited samples.

The main aim of this paper is to improve the estimation of the intrinsic UV LF at high redshift by developing a formalism to take into account the magnification bias. Our new formalism improves on previous work in several ways: we extend the analytic strong lensing model of Wyithe et al. (2011) to include the redshift evolution of the deflector population, and we develop a technique to treat the intermediate lensing regime and introduce a framework to include weak lensing effects, neither of which have been systematically accounted for in any previous estimates of the LF. Furthermore, by providing probability distribution functions for the magnification of each dropout and empty field, our formalism can be directly included in any Bayesian LF parameter estimation, thus allowing for a rigorous derivation of the related uncertainties.

We present two applications of our formalism. The first application is the interpretation of the  $z \sim 8$  dropouts found by the *Brightest of Reionizing Galaxies Survey*<sup>1</sup>, (hereafter BoRG, Trenti et al. 2011). After estimating the fraction of sources in BoRG that are multiply imaged and presenting one strongly-lensed candidate and three candidate systems with magnification  $\mu > 1.4$ , we use the extended sample presented by Schmidt et al. (2014a) to derive the LF including the effects of magnification bias. For this we extend the Bayesian formalism introduced by Schmidt et al. (2014a) by including a term describing the likelihood for magnification of high-redshift sources for each field, and marginalize over the range of possible magnifications.

The second application of our formalism is a set of predictions for the modification of the LF at  $8 < z \leq 16$  by using a variety of possible LFs based on theoretical models (Muñoz 2012, Behroozi et al. in preparation) and extrapolations of lower redshift data (Bouwens et al. 2014; Finkelstein et al. 2014). With our formalism we can give a quantitative assessment of how magnification bias will affect future surveys.

The paper is organized as follows. In Section 2 we briefly describe the BoRG survey and the data used in this paper. In Section 3 we introduce the relevant the-

oretical background for gravitational lensing and magnification bias. In Section 4 we develop a semi-analytic framework, based on that in Wyithe et al. (2011) to study the magnification bias due to strong and intermediate gravitational lensing. In Section 5 we use the reconstruction of lines-of-sight in cosmological simulation data to investigate weak lensing. The Bayesian inference for the determination of the intrinsic LF is introduced in Section 6 and presented in more detail in Appendix A. The results are presented and discussed in Section 7. A brief summary is given in Section 8.

All magnitudes are AB magnitudes and a standard concordance cosmology with  $\Omega_m = 0.3$ ,  $\Omega_\Lambda = 0.7$ , and  $h = 0.7$  is assumed. The Millennium Simulation uses a cosmology with  $\Omega_m = 0.25$ ,  $\Omega_\Lambda = 0.75$ , and  $h = 0.73$ , which is used to estimate the weak lensing magnification. We assume the difference between these two cosmologies is negligible for our purposes.

## 2. DATA

This paper estimates the  $z \sim 8$  LF using 38 bright Lyman Break galaxies selected from the BoRG survey and 59 fainter dropouts taken from deep legacy fields (in HUDF09 and the WFC3/IR wide area Early Release Science). The BoRG survey is described briefly in Section 2.1, but we refer to Trenti et al. (2011, 2012); Bradley et al. (2012) and Schmidt et al. (2014a) for further details. The deep legacy data are described by Bouwens et al. (2011). Additionally, we used data of galaxies with spectroscopically determined velocity dispersions to estimate the velocity dispersion of the foreground BoRG galaxies (described in Section 2.2). In Section 2.3 we give an overview of the simulated data used in the analysis of weak lensing.

### 2.1. The BoRG Survey

The ongoing BoRG survey is a pure-parallel imaging program with the HST WFC3. The current survey covers  $\sim 350$  arcmin<sup>2</sup> divided into 71 independent fields located randomly on the sky. This reduces cosmic variance below the level of statistical noise (Trenti & Stiavelli 2008; Bradley et al. 2012). The photometry is in the visual and near-infrared, primarily using the four HST WFC3 filters F606W, F098M, F125W, and F160W (commonly referred to as V-, Y-, J-, and H-bands respectively). The  $z \sim 8$  BoRG survey consisted mainly of HST programs GO/PAR 11700 and GO/PAR 12572 (PI: Trenti) and includes a small additional number of coordinated parallels from COS-GTO. 53 core BoRG fields are complemented by other archival data including 8 fields from GO/PAR 11702 (PI: Yan, Yan et al. 2011) and 10 COS-GTO fields, which used the F600LP-band instead of the F606W-band. The BoRG survey is the largest current survey of Y-band dropouts by solid angle.

The  $z \sim 8$  galaxy candidates were identified from Y-band dropouts, full details of the dropout technique (Madau 1995) are described in Schmidt et al. (2014a). The BoRG survey detected 38 Lyman break galaxy (LBG) candidates at  $z \sim 8$  with  $S/N > 5$  in the J-band, of which 10 have  $S/N > 8$  (Bradley et al. 2012; Schmidt et al. 2014a). We use the  $5\sigma$  sample of objects in this work.

### 2.2. Massive Foreground Galaxies Acting as Deflectors

<sup>1</sup> <http://borg.physics.ucsb.edu>

In Section 4.2 we estimate the velocity dispersions of strong lens candidates in the BoRG fields by comparing their photometry with similar early-type galaxies which have both HST photometry and spectroscopically determined velocity dispersions. We divided the galaxy samples into three large redshift bins in order to account for the position of the 4000Å break in the filters at higher redshifts.

In the range  $z < 1$  we used a sample of 165 spheroidal galaxies from Treu et al. (2005) with photometry from the Great Observatories Origins Deep Survey North (GOODS-N, Bundy et al. 2005). For  $z > 1$  we use a sample of 66 massive quiescent galaxies, presented by Belli et al. (2014a,b), which were selected from HST photometric catalogs of objects in the COSMOS, GOODS and Extended Groth Strip (EGS) fields (Grogin et al. 2011; Koekemoer et al. 2011; Windhorst et al. 2011). We used an aperture correction to rescale observed velocity dispersions,  $\sigma_{\text{obs}}$ , to  $\sigma_e$ , the velocity dispersion within one effective radius,  $R_e$ . We follow Belli et al. (2014a) and used the model of van de Sande et al. (2013) which proposes a constant rescaling:

$$\sigma_e = 1.05\sigma_{\text{obs}} \quad (1)$$

For galaxies at  $z < 1$  (the Treu et al. (2005) sample), we used the model of Cappellari et al. (2006):

$$\sigma_e = \left(\frac{R_e}{R}\right)^{-0.066} \sigma_{\text{obs}} \quad (2)$$

where the slit size,  $R$  is the 1'' aperture on Keck DEIMOS (Treu et al. 2005).

The reference photometry used for the individual samples differ. As listed in Table 1 we use HST F606W for galaxies at  $z < 0.5$ , HST F850LP from Treu et al. (2005) (converted to F098M through linear interpolation) for galaxies at  $0.5 < z < 1.0$ , and HST F160W for galaxies at  $z > 1$ .

### 2.3. The Millennium Simulation

In Section 5 we describe our method to generate weak lensing PDFs by reconstructing simulation data along the line-of-sight to  $z \sim 8$ . Due to the very high redshift of our sources, it was necessary to use simulation data containing halos out to redshifts above 5.

We used 24  $1.4 \times 1.4$  square degree simulated lightcones built by Henriques et al. (2012) from the Millennium Simulation (Springel et al. 2005) which contain halos out to  $z \sim 12$ . While the Millennium Simulation contains halos from very high redshift, it has a box length of only 500 Mpc  $h^{-1}$ . The comoving distance in the universe to  $z = 1$  is 2390 Mpc  $h^{-1}$ , so it is necessary to build lightcones with the galaxies correctly distributed in comoving volumes (see Blaizot et al. (2005) and Kitzbichler & White (2007) for a thorough discussion of generating mock lightcones).

These lightcones were generated using the semi-analytical galaxy formation model of Guo et al. (2011), and photometric properties were calculated using the stellar population synthesis code by Maraston (2005).

## 3. THEORETICAL BACKGROUND

In this section we summarize the relevant theory for the galaxy LF, strong and weak gravitational lensing, and magnification bias.

### 3.1. Galaxy Luminosity Function

When a simply parametrized form is needed, we describe the LF by a Schechter function (Schechter 1976):

$$\Psi(L) = \frac{\Psi^*}{L^*} \left(\frac{L}{L^*}\right)^\alpha \exp\left(-\frac{L}{L^*}\right) \quad (3)$$

where  $L^*$  marks the characteristic break in the LF,  $\Psi^*$  is the characteristic density at that luminosity and  $\alpha$  is the power-law exponent slope of the faint end.

### 3.2. Strong Lensing

If the line-of-sight to a background source is closely aligned with a massive foreground object, e.g. a cluster or single massive galaxy, gravitational lensing can produce multiple observed images of the source (Schneider et al. 1992, 2006). Multiple imaging signifies the regime of strong gravitational lensing.

#### 3.2.1. Singular Isothermal Sphere

Strong gravitational lenses are commonly modeled as Singular Isothermal Spheres (SIS), which provides a convenient analytic form to describe the mass profiles of massive galaxies (e.g. Treu 2010, and references therein). The scale of image separation is characterized by the *Einstein radius* of the lens:

$$\theta_{\text{ER}}(\sigma, z) = 4\pi \frac{D_{ls}}{D_s} \left(\frac{\sigma}{c}\right)^2 \quad (4)$$

where  $D_{ls}$  and  $D_s$  are the angular diameter distances between the lens and source, and from the observer to the source respectively,  $\sigma$  is the velocity dispersion of the lens galaxy, and  $c$  is the speed of light. Velocity dispersion is the most important property for determining the strength of a strong gravitational lens as it scales with the mass of the dark matter in the system (Turner et al. 1984; Schneider et al. 2006; Treu 2010).

The magnification,  $\mu$ , due to an SIS lens is given by:

$$\mu = \frac{|\theta|}{|\theta| - \theta_{\text{ER}}} \quad (5)$$

where  $\theta$  is the distance between the lens and the source in the image plane. An SIS lens can produce two images, with the brighter one having magnification  $\mu > 2$ , or one image with magnification  $\mu < 2$ . The case of multiple imaging is referred to here as strong lensing. In this paper we refer to images with  $1.4 < \mu < 2$  as intermediate lensing.

#### 3.2.2. Multiple Image Optical Depth

The optical depth  $\tau_m$  is the cross-section for a galaxy at redshift  $z_S$  to be multiply imaged (i.e. strongly lensed) by a foreground galaxy at  $z_L$ : it is the fraction of the sky covered by the Einstein radii of all intervening deflectors at redshifts  $z_L$ . Following standard practice and assuming SIS deflectors, Wyithe et al. (2011) defines it as:

$$\tau_m = \int_0^{z_S} dz_L \int d\sigma \Phi(\sigma, z_L) (1+z_L)^3 c \frac{dt}{dz_L} \pi D_L^2 \theta_{\text{ER}}^2(\sigma, z_L) \quad (6)$$

where  $\Phi(\sigma, z_L)$  is the velocity dispersion function of the deflectors,  $D_L$  is the angular diameter distance to  $z_L$ , and  $t$  is time. Without the magnification bias, the optical depth gives the probability of a high-redshift source being multiply imaged.

### 3.3. Weak Lensing

Weak gravitational lensing is the deflection of light that causes the magnification and distortion of an observed source, but without producing multiple images. There are no empty lines-of-sight in the universe, so all light traveling to us has been deflected some amount by intervening mass (Hilbert et al. 2007). Whilst it is impossible to determine the exact effect on individual observed sources, it can be done in a statistical sense and is important to quantify this effect for our high-redshift sources.

The lens equation can be constructed for an arbitrary number of lens planes due to an ensemble of deflectors along the line-of-sight (Hilbert et al. 2009; McCully et al. 2014). The magnification of a source in a multiplane system is a function of the total convergence and total shear experienced. Hilbert et al. (2009) showed to first order that the total convergence and shear are the sum of the individual contributions from each object along the line-of-sight:

$$\mu = \frac{1}{(1 - \sum_i \kappa_i)^2 - |\sum_i \gamma_i|^2} \quad (7)$$

The convergence,  $\kappa_i$ , and shear,  $\gamma_i$ , of each object are determined by the lens model.

### 3.4. Magnification Bias

The gravitational lensing of a source with luminosity  $L$  in a solid angle  $\Omega$  of sky has two effects. The observed luminosity is magnified by a factor  $\mu$  and sources are now distributed over a magnified solid angle  $\mu\Omega$ . In a flux-limited sample intrinsically low luminosity sources can be magnified above the survey limit, while the number density of sources can decrease for a given observed solid angle.

Since the faint end of the LF of high-redshift LBG galaxies is so steep, in regions around large low-redshift deflectors we may observe an excess of intrinsically faint high-redshift sources. These effects are known as the *magnification bias* and will effect our inferences about the population and LF of high-redshift galaxies.

If it were possible to observe all galaxies in the universe without the magnification bias the probability of a high-redshift galaxy being strongly lensed is purely given by the optical depth,  $\tau_m$  (Section 3.2.2). However, magnification of more numerous intrinsically faint sources into our surveys implies that we do not observe the true population of galaxies with luminosity. The magnification bias increases the probability that a sample of observed high-redshift sources have been gravitationally lensed.

The magnification bias for sources with observed luminosities above  $L_{\text{lim}}$  in a flux-limited sample is given

by:

$$B = \frac{\int_{\mu_{\text{min}}}^{\mu_{\text{max}}} d\mu p(\mu) N(> \frac{L_{\text{lim}}}{\mu})}{N(> L_{\text{lim}})} \quad (8)$$

assuming that each source could be magnified between  $\mu_{\text{min}}$  and  $\mu_{\text{max}}$ . Where  $p(\mu)$  is the probability distribution for magnification of a source and  $N(> L_{\text{lim}})$  is the integrated galaxy LF (Wyithe et al. 2011).

The true probability of a high-redshift source being multiply imaged is  $B\tau_m$ . Therefore, using  $B$  it is possible to find the fraction of galaxies at a given redshift in a flux-limited sample that are multiply-imaged:

$$F_{\text{mult}} = \frac{B\tau_m}{B\tau_m + B'(1 - \tau_m)} \quad (9)$$

We assume that  $B'$ , the bias for galaxies to not be multiply imaged is close to unity.

If the survey limit is brighter than the characteristic apparent magnitude of the observed sample the magnification bias is expected to be large, as a large fraction of the observed sources are likely to be intrinsically fainter sources magnified above the detection threshold of the survey.

We can compute the gravitationally lensed LF, including strong and weak gravitational lensing:

$$\Psi_{\text{mod}}(L) = (1 - \tau_m) \frac{1}{\mu_{\text{demag}}} \Psi\left(\frac{L}{\mu_{\text{demag}}}\right) + \tau_m \int_0^\infty d\mu \frac{1}{\mu} p(\mu) \Psi\left(\frac{L}{\mu}\right) \quad (10)$$

Where  $\mu_{\text{demag}} < 1$  is introduced such that the mean magnification over the entire sky is unity (Pei 1995; Wyithe et al. 2011) and  $p(\mu)$  is the full probability density for magnification of a high-redshift source, as above.

## 4. STRONG AND INTERMEDIATE LENSING

In this section we compute the probability that the  $z \sim 8$  dropouts are affected by strong and intermediate lensing. First, in Section 4.1 we compute the strong lensing optical depth and the probability that a  $z \sim 8$  source is multiply imaged by foreground massive elliptical galaxy deflectors. We account for evolution of the deflector population based on the observed stellar mass function. In Section 4.2 we describe our method to identify sources in the intermediate lensing regime ( $1.4 < \mu < 2$ ). In order to identify these sources, we estimate the lensing strength of massive foreground galaxies based on HST photometry and an empirical calibration of the Faber & Jackson (1976) relation. A candidate strongly lensed dropout in the BoRG fields was presented by Barone-Nugent et al. (2013), in this paper one more candidate multiply-imaged dropout ( $\mu > 2$ ) is found, and three dropouts may experience significant intermediate magnification. We detail their properties in Table 2.

### 4.1. Strong Lensing by an Evolving Deflector Population

In order to compute the strong lensing optical depth and multiple image probability, we follow Wyithe et al. (2011) and use a simple SIS lensing model (see Section 3.2.1) with a flat cosmology. Strong lenses are assumed to be uniformly distributed in the universe and

we can calculate the probability of encountering a strong lens along the line-of-sight to a high-redshift source, i.e. the lensing optical depth (see Section 3.2.2). By considering the number of galaxies observed above a certain flux limit we can calculate the magnification bias factor,  $B$ , from Equation (8), assuming a Schechter luminosity function (Equation (3)). For these calculations we use the  $z \sim 8$  LF inferred by Schmidt et al. (2014a), with a characteristic magnitude of  $M^* = -20.15^{+0.29}_{-0.38}$ , faint-end slope of  $\alpha = -1.87^{+0.26}_{-0.26}$ , and number density of  $\log_{10} \Psi^* [\text{Mpc}^{-3}] = -3.24^{+0.25}_{-0.24}$ . We marginalize over the entire MCMC chain for each of the Schechter parameters.

In their calculation of the optical depth Wyithe et al. (2011) used the local velocity dispersion function as measured by SDSS (Choi et al. 2007). As most strong lenses occur at  $z \lesssim 1.5$  (Fassnacht et al. 2004; Treu 2010), Wyithe et al. (2011) assumed that the velocity dispersion function does not evolve with redshift for massive galaxies. This is consistent with studies of the velocity dispersion function out to  $z \sim 1$  (e.g., Chae 2010; Bezanson et al. 2012). However, significant galaxy growth and evolution is observed from  $z > 1$  as structure forms (van de Sande et al. 2013; Belli et al. 2014a), and we can improve the accuracy of the model by allowing the parameters of the velocity dispersion function for massive ellipticals to evolve with redshift. Introducing redshift evolution is expected to reduce the optical depth (Barkana & Loeb 2000).

The dashed blue line in the left panel of Figure 3 shows the probability that the source has been multiply imaged as a function of lens redshift for a source at  $z \sim 8$ , calculated using Equation (6). The distribution is strongly peaked at  $z_L \sim 1$ , but there is a significant probability that  $z_L > 1.5$ . Only 48% of the contribution to the optical depth for strong lensing occurs at  $z_L < 1.5$ . We find that 90% of lensing occurs within a lens redshift of  $z_L \lesssim 3.5$ . Therefore, in order to account for most of the optical depth we need to find the form of the velocity dispersion function out to  $z = 3 \sim 4$  where the galaxy population is significantly different from recent times (Bundy et al. 2005; Muzzin et al. 2013; van de Sande et al. 2014).

Several studies have investigated the evolution of the velocity dispersion function out to  $z \sim 1.5$  (e.g., Chae 2010; Bezanson et al. 2011, 2012, 2013). These works are consistent with no evolution, but have large uncertainties. Measurements of velocity dispersion beyond  $z > 2$  are very difficult as the brightest emission lines fall within near-IR atmospheric absorption regions (Kriek et al. 2006; Belli et al. 2014b).

Therefore, we estimate the evolution of the velocity dispersion function at high redshift based on the evolution of the stellar mass function, a related quantity that has been well-measured at  $z > 2$ . We convert the stellar mass function into the velocity dispersion function by means of the well-known correlation between stellar velocity dispersion ( $\sigma$ ) and stellar mass ( $M_{\text{stell}}$ ) taken from Auger et al. (2010):  $\log(\sigma [\text{km s}^{-1}]) = p\bar{M} - 11p + q$ , where  $p = 0.24 \pm 0.02$ ,  $q = 2.34 \pm 0.01$  and  $\bar{M} = \log(M_{\text{stell}}/M_{\odot})$ . This relation was derived for massive lens galaxies with high velocity dispersions, which will be the strongest contribution to the optical depth as  $\tau \sim \sigma^4$ .

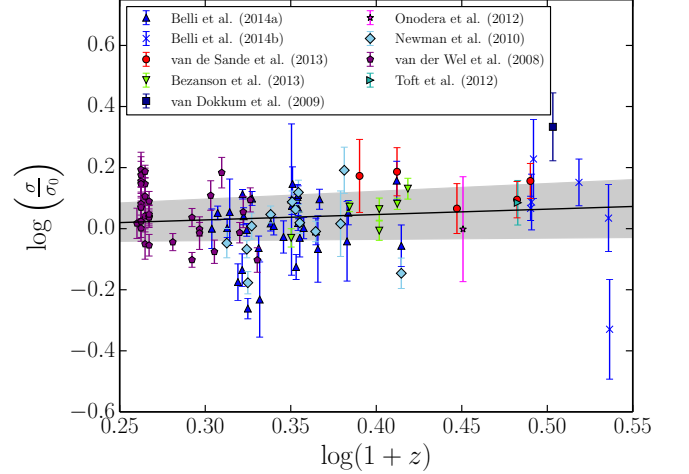


FIG. 1.— Redshift evolution of massive galaxy velocity dispersion, relative to the velocity dispersion estimated from inferred stellar masses via the Auger et al. (2010) relation. We find evolution of the form  $\log(\sigma/\sigma_0) \propto (1+z)^{0.18 \pm 0.15}$ , where  $\sigma_0$  is the velocity dispersion estimated using the stellar mass-velocity dispersion relation from Auger et al. (2010). We plot the mean linear fit (black line) and the  $1\sigma$  confidence region (gray shaded region).

High-redshift galaxies are observed to have higher velocity dispersions at fixed mass than in the local universe (e.g., van de Sande et al. 2013; Belli et al. 2014a; Bezanson et al. 2014). Thus the stellar mass-velocity dispersion relation is expected to evolve with redshift. Following van de Sande et al. (2013) we expect evolution of the form  $\log(\sigma/\sigma_0) \propto (1+z)^\beta$ . In Figure 1 we plot publicly available data from van der Wel et al. (2008); van Dokkum et al. (2009); Newman et al. (2010); Toft et al. (2012); Bezanson et al. (2013); van de Sande et al. (2013); Belli et al. (2014a,b) and fit a relation of this form for all galaxies with estimated stellar masses between  $10.8 < \log(M_{\text{stell}}/M_{\odot}) < 12.0$  as this was the region where the Auger et al. (2010) relation was derived. We find  $\beta = 0.18 \pm 0.15$ , the large uncertainty is due to scatter in velocity dispersion measurements at  $z > 1.5$ , and the large uncertainty in these measurements. Our result is slightly lower than the result from van de Sande et al. (2013) which did not include the data from Belli et al. (2014a,b). We use the Auger et al. (2010) stellar mass-velocity dispersion relation which is for massive lens galaxies as the  $z \sim 0$  expected velocity dispersion, whereas van de Sande et al. (2013) use a relation derived from the full range of galaxies in the SDSS. We note that because the optical depth depends on velocity dispersion to the fourth power, the form of the velocity dispersion function at  $z > 2$  is the greatest source of uncertainty in the calculation of optical depths.

The stellar mass function can be described by a Schechter function (e.g., Muzzin et al. 2013):

$$\Phi_S(\bar{M}) = (\ln 10) \Phi_S^* 10^{(\bar{M} - \bar{M}_S^*)(1 + \alpha_S)} \exp \left[ -10^{\bar{M} - \bar{M}_S^*} \right] \quad (11)$$

The characteristic stellar mass is given by  $\bar{M}_S^* = \log(M_{\text{stell}}^*/M_{\odot})$ ,  $\Phi_S^*$  is the characteristic density normalization, and  $\alpha_S$  is the low-mass-end slope.

In order to model the redshift evolution of the stellar mass function, we use publicly available data on quies-



cent galaxies at  $z \leq 4$  from the COSMOS/UltraVISTA Survey (Muzzin et al. 2013). They derive the best-fit single Schechter function parameters for the stellar mass function as a function of redshift. Their stellar mass function parameters for quiescent galaxies, allowing for evolution of  $\alpha_S$ , are plotted as a function of redshift in Figure 2. We assumed the redshift evolution  $X = X_0(1+z)^a$ , where  $X$  represents the stellar mass function Schechter parameters and  $X_0$  represents the values at  $z = 0$ .

We used a Bayesian MCMC linear fitting method to fit this functional form to the data, and plot the mean and one standard deviation confidence fits in Figure 2. There is significant evolution in  $\Phi_M^*$ . However, there is also large uncertainty in the evolution of  $\Phi_M^*$  due to the uncertainty in high-redshift measurements. We ignore evolution in the low-mass-end slope, since the lensing effect is dominated by the most massive galaxies. We also ignore evolution in  $\bar{M}_S^*$ , for which the evolution appears non-negligible but it has little effect on Equation (11). The redshift-dependent velocity dispersion function obtained in this way becomes

$$\Phi(\sigma, z) = p^{-1} \frac{\Phi_S^*(z)}{\sigma(1+z)^\beta} \left(\frac{\sigma}{\sigma^*}\right)^{p^{-1}(1+\alpha_S)} \exp\left[-\left(\frac{\sigma}{\sigma^*}\right)^p\right] \quad (12)$$

with  $p = 0.24 \pm 0.02$ ,  $\beta = 0.18 \pm 0.15$  (obtained from the evolution of velocity dispersion in Figure 1),  $\Phi_S^*(z) = 3.75 \pm 2.99 \times 10^{-3}(1+z)^{-2.46 \pm 0.53} \text{ Mpc}^{-3}$ ,  $\alpha_S = -0.54 \pm 0.32$  and  $\sigma^* = 216 \pm 18 \text{ km s}^{-1}$ . This was derived using the stellar mass-velocity dispersion relation above (Auger et al. 2010), including the scatter in the relation. At  $z = 0$  recent well-measured velocity dispersion functions (e.g., Sheth et al. 2003; Choi et al. 2007) are within the uncertainties of this redshift-evolving relation, showing that our inferred evolution is consistent with direct measurements where they overlap.

Using this redshift-dependent velocity dispersion function we compute the optical depth for strong lensing, and the distribution of the optical depth with lens redshift. In the left panel of Figure 3, now using the redshift evolving deflector population from Equation (6) and Equation (12), we see that the majority of the contribution to the optical depth is from lens galaxies at  $z \lesssim 1.5$ , which agrees with current observations of lensed high-redshift dropouts (Barone-Nugent et al. 2013; Schmidt et al. 2014b; Atek et al. 2014). In the right panel of Figure 3 we plot the optical depth as a function of source redshift and find that including the redshift evolution of the deflector population reduces the optical depth at high redshift compared with the work in Wyithe et al. (2011) as expected by theoretical predictions (Barkana & Loeb 2000), and it appears to start to flatten by  $z_S \sim 10$ .

Our estimated optical depth at  $z < 8$  is in good agreement with values derived by an independent method by Barone-Nugent et al. (2015, in preparation), and consistent with Wyithe et al. (2011) for  $z \lesssim 8$ . We note the optical depths presented in Barone-Nugent et al. (2015, in preparation) are marginally higher than the results of this paper, but we can recover their optical depth using a steeper evolution of  $\sigma(z)$ . It is clear that the uncertainty in the evolution of velocity dispersion, which is the best

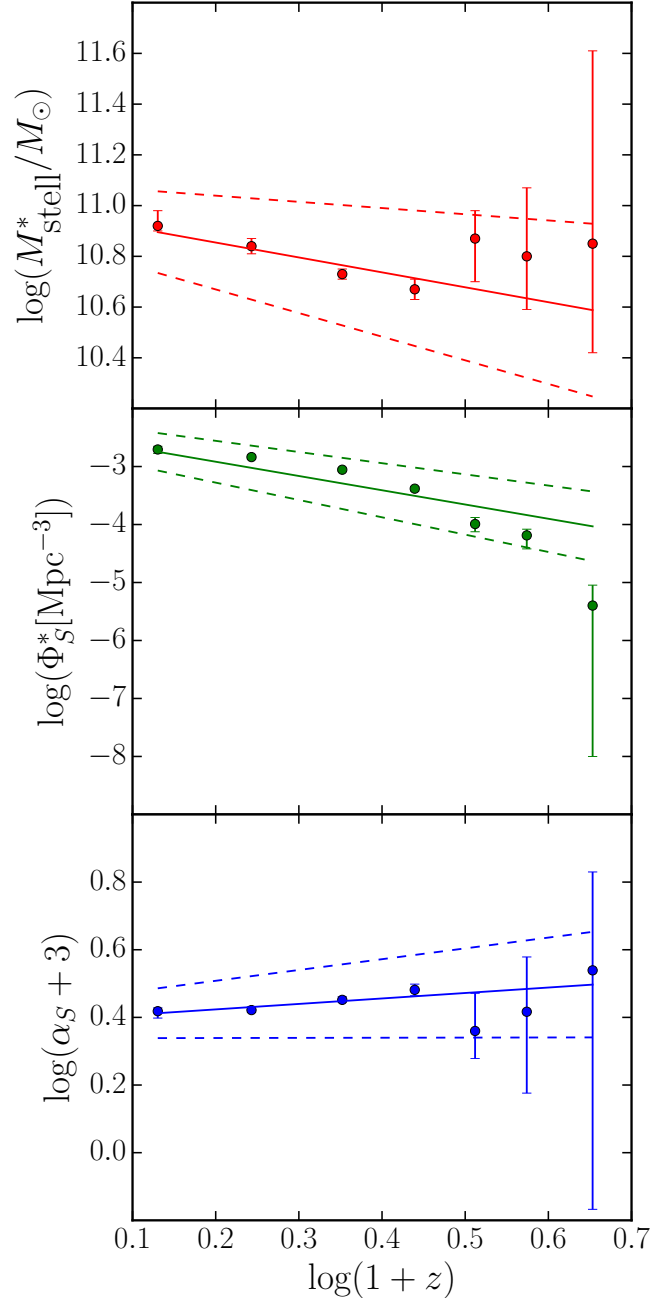


FIG. 2.— Redshift evolution of the best-fit single Schechter function parameters from Muzzin et al. (2013) for the stellar mass function of quiescent galaxies, allowing for evolution of  $\alpha_S$ . Fits of the form  $X_0(1+z)^a$  are plotted: the solid lines show the mean fit, dotted lines show the  $1\sigma$  error on the data. Only  $\Phi_M^*$  shows significant evolution with redshift.

indicator of the mass of lens galaxies, provides the largest uncertainty in determining the optical depth.

Finally, we compute the probability that high-redshift galaxies in a flux-limited sample have been multiply imaged. This is shown in Figure 4 as a function of limiting magnitude for each of the BoRG fields. As expected, the probability that a source in each field is multiply imaged,  $F_{\text{mult}}$  (Equation (9)) increases with the survey limiting magnitude, owing to the magnification bias. We estimate 3-15 % of observed sources brighter than  $M^*$  have

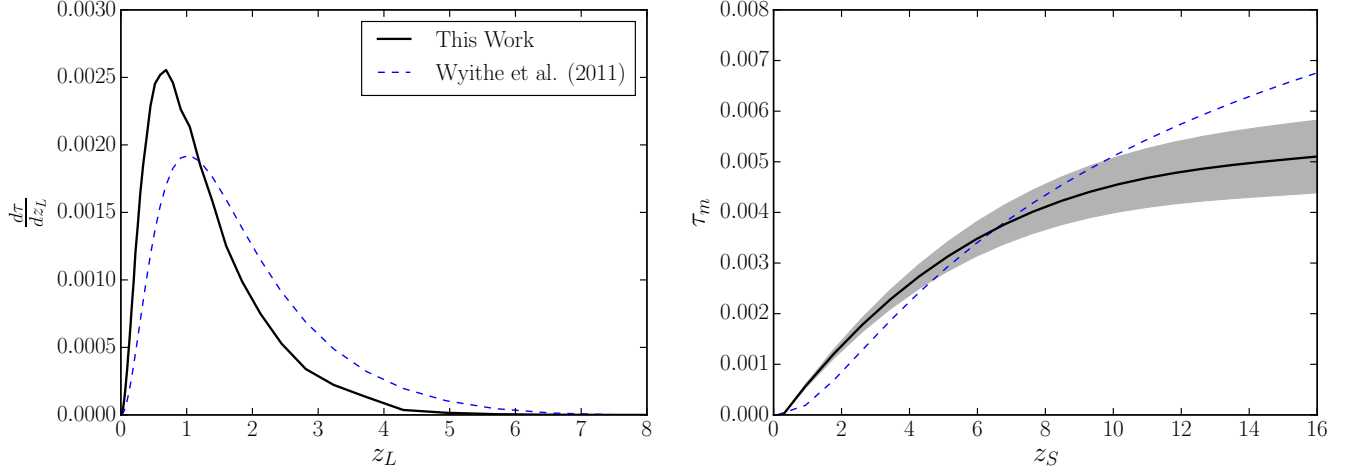


FIG. 3.— **(Left)** Contribution to the optical depth for a source at  $z \sim 8$  to be multiply imaged as a function of the lens redshift,  $z_L$ , (solid black line) calculated using Equation (6), including the evolution of the deflector population with redshift (Section 4.1), for comparison we plot the contribution for a constant comoving density of lens galaxies (dashed blue line, Wyithe et al. 2011). **(Right)** Optical depth for multiple imaging as a function of source redshift, including evolution of the deflector population (solid black line). The optical depth without redshift evolution of lens galaxies is also plotted for comparison (dashed blue line, Wyithe et al. 2011).

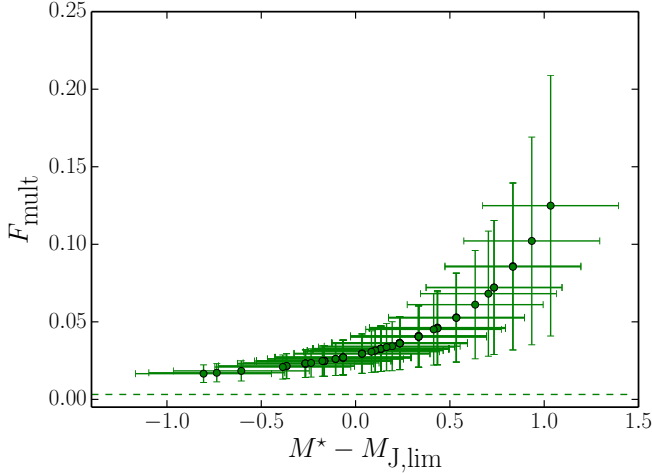


FIG. 4.— Multiply-imaged fraction (see Equation (9)) for  $z \sim 8$  sources brighter than the J-band limiting magnitude in each of the BoRG fields, as a function of the UV characteristic magnitude,  $M^*$ , including the evolution of the deflector population (Section 4.1). The probability of a high-redshift source being multiply imaged increases as the survey magnitude limit becomes brighter than  $M^*$ . We expect very few intrinsically bright sources, so any bright source has a high likelihood of being significantly magnified according to the magnification bias. We have used the full MCMC chain for  $M^*$  from Schmidt et al. (2014a) and plot the mean value with errorbars of one standard deviation. The optical depth, the probability of multiple imaging without including the magnification bias factor,  $B$  (Section 3.4), is plotted as the green dashed line.

been strongly lensed, this is consistent with the results of Barone-Nugent et al. (2015, in preparation) who use an independent method to infer the lensed fraction.

#### 4.2. Identifying Significantly Magnified Sources

Whilst all the fields are subject to weak lensing, it is necessary to establish which of the individual sources experience multiple-imaging ( $\mu > 2$ ), or are close enough to a deflector to experience an intermediate magnification ( $1.4 < \mu < 2$ ). We expect strong lensing events to be rare, but possible given the size of the BoRG survey. Among the BoRG sources, Barone-Nugent et al. (2013) presented

a candidate strongly-lensed system in borg\_0440-5244 (for naming conventions see Bradley et al. 2012). The candidate appears to be lensed by a foreground group with an Einstein radius of  $1.49''$ , corresponding to a velocity dispersion of  $\sim 300 \text{ km s}^{-1}$ , producing a magnification of  $3.7 \pm 0.2$  of the dropout. In this Section we describe a method to identify other potentially lensed sources in the catalogs and illustrate how to account for them systematically when estimating the LF.

For computational speed, we considered as potential deflectors only  $z < 3$  objects within 18 arcseconds of the  $z \sim 8$  dropouts in each field (the typical Einstein radius is of order 1-2 arcseconds for massive galaxies). The key quantity that we need to estimate the lensing strength is the velocity dispersion (Turner et al. 1984; Treu 2010). Thus for every galaxy sufficiently close to a dropout, we estimate their velocity dispersions by comparing their photometry with that of samples of similar objects with spectroscopically-determined velocity dispersions. We selected galaxy samples with HST photometry in bands used in BoRG in order to estimate velocity dispersion based on our own photometry. As a comparison sample, we used data from Treu et al. (2005) and Belli et al. (2014a,b), as described in Section 2.2.

As described in Section 4.1, the velocity dispersion-stellar mass relation is believed to evolve weakly with redshift since since  $z \sim 2$  (e.g., van de Sande et al. 2013; Belli et al. 2014b; Bezanson et al. 2014), and galaxies will be intrinsically brighter at higher redshift due to younger stellar populations (e.g. Treu et al. 2005). We account for this by fitting an evolving Faber & Jackson (1976) relation to the comparison sample of the form  $L \propto \sigma^4(1+z)^\beta$ .

In practice, we bin the data in redshift, and fit a function of the form  $\log \sigma = -0.1m + a \log(1+z) + b$  using a Bayesian MCMC estimation where  $\sigma$  is the velocity dispersion in  $\text{km s}^{-1}$ ,  $m$  is apparent magnitude in a given band,  $z$  is galaxy redshift, and  $a$  and  $b$  are constants. We restrict our fit to galaxies with a measured velocity dispersion of at least  $200 \text{ km s}^{-1}$ , where samples are less affected by incompleteness and selection effects. We

present the estimated parameters in Table 1 and fits to the data are shown in Figure 5.

TABLE 1  
CORRELATION BETWEEN VELOCITY DISPERSION, REDSHIFT AND APPARENT MAGNITUDE

Redshift	Band ( $m$ )	a	b
$z < 0.5$	F606W	$2.26 \pm 0.79$	$4.08 \pm 0.12$
$0.5 < z < 1.0$	F089M	$0.93 \pm 0.13$	$4.20 \pm 0.03$
$z > 1.0$	F160W	$1.02 \pm 0.15$	$4.12 \pm 0.05$

NOTE. – Fits of the form  $\log \sigma = -0.1m + a \log(1 + z) + b$

The posterior probability distribution function of Einstein radii for each object are found using Equation (4), sampling over the full MCMC chain for the velocity dispersion. The redshifts of the objects were determined using the Bayesian Photometric Redshifts (BPZ) code (Benitez et al. 2004; Coe et al. 2006). The PDF for magnification,  $p(\mu)$  is found by computing the magnification,  $\mu$  (Equation (5)), at the position of the dropout given the distribution of Einstein radii found for each foreground object using the distribution for its velocity dispersion,  $\sigma_{\text{inf}}$  estimated from the fits in Table 1. The greatest source of error in this procedure is the magnitude-velocity dispersion-redshift relation: errors in magnitude and redshift determination are negligible.

When the mean magnification produced by such a foreground object exceeds  $\mu = 1.4$  we use the magnification PDF derived from the above procedure and treat the dropout as described in Section 6.2.2 in our calculations of the LF.

Using this method, we find one of the dropouts (borg\_0436-5259\_1233, presented in Bradley et al. 2012) has a magnification probability distribution consistent with strong lensing. This dropout is shown in the top left panel of Figure 6 and its estimated lensing properties are given in Table 2. The dropout appears to be magnified by a large galaxy at  $z \sim 0.40$  with estimated velocity dispersion  $294 \pm 47 \text{ km s}^{-1}$  (estimated from photometry via the empirical relation presented in Table 1). We estimate its magnification to be  $\mu = 2.05 \pm 0.52$ , the large uncertainty is due to the uncertainty in the relationship between apparent magnitude and velocity dispersion. The dropout is very faint ( $m_J = 27.0 \pm 0.2$ ) and no significant elongation is detected in any of the observed bands but this dropout would be an excellent object for further investigation.

Three of the dropouts (borg\_1301+0000\_160, borg\_1408+5503 and borg\_2155-4411\_341) experience mean magnification  $> 1.4$ . Postage stamps of these dropouts are shown in Figure 6 and their lensing properties are presented in Table 2. Interestingly, borg\_1301+0000\_160 is the brightest dropout in the survey, with  $m_J = 25.5$ , and appears tangentially elongated in the J-band image (middle panel of Figure 6). This object is also a very interesting target for further imaging and spectroscopic follow-up.

We note that our method assigns a significantly lower velocity dispersion to the potential strong lens (borg\_0440-5244\_647) than the one estimated by Barone-Nugent et al. (2013) in their presentation of this object. They estimated the velocity dispersion of the deflector to be  $\sigma \sim 300 \text{ km s}^{-1}$ , whereas our method estimates a

mean velocity dispersion of  $\sim 170 \pm 33 \text{ km s}^{-1}$ . This is likely to be because our method does not account for lensing by groups and clusters, while Barone-Nugent et al. (2013) suggest that this dropout is lensed by a group of at least two objects at  $z \sim 1.8$ , of which borg\_0440-5244\_647 is the largest. They estimated velocity dispersions of the deflector galaxies by using an abundance matching relation between mass and luminosity, derived from Cooray (2005), and measuring the angular size of the lensing objects. However, when using a redshift-dependent Faber & Jackson (1976) relation (Barone-Nugent et al. 2015, in preparation) similar to ours (Table 1) they estimate the velocity dispersion of this single galaxy to be  $\sim 180 \pm 46 \text{ km s}^{-1}$  (via private communication), which agrees with our result. Neglecting group-scale lensing is a potential limitation of our method, which may underestimate magnification in a few cases. However the impact on the overall estimation of the LF inference is negligible since the phenomenon is so rare.

## 5. WEAK LENSING

In this section we discuss the methods used to find the PDFs for magnification of a source at  $z \sim 8$  by all intervening matter. We used the Pangloss code<sup>2</sup> developed by Collett et al. (2013) that generates lensing parameters for reconstructed lines-of-sight. We describe the production of magnification PDFs from simulation data from the Millennium Simulation (Springel et al. 2005) in Section 5.1 and in Section 5.2 we present the BoRG field weak magnification PDFs. Our PDFs agree well with other theoretical work at lower redshifts (Hilbert et al. 2007, 2009; Greene et al. 2013).

### 5.1. Estimating Magnification from Simulation Catalogs

The weak lensing reconstruction model developed by Collett et al. (2013) takes simulation halo catalogs and places halos in a three-dimensional grid, with each halo contributing convergence  $\kappa_i$  and shear  $\gamma_i$  along a line-of-sight to a source at a given redshift. Halos are modeled as truncated NFW profiles (Baltz et al. 2009):

$$\rho(r) = \frac{\rho_{\text{NFW}}(r)}{1 + \left(\frac{r}{r_t}\right)^2} \quad (13)$$

where we used the truncation radius  $r_t = 5r_{200}$ , shown to be robust by Collett et al. (2013). Where  $r_{200}$  is the radius at which the mass density falls to 200 times the critical mass density of the universe. The convergence and shear derived from this profile are given in Baltz et al. (2009). Magnification due to all intervening deflectors along a line-of-sight is given by Equation (7).

We built PDFs for all lensing parameters by sampling over  $10^3$  of lines-of-sight. As described in Section 2.3 we used lightcones built from the Millennium Simulation (Henriques et al. 2012; Springel et al. 2005).

The simulated catalogs provide a list of halos with associated galaxies, but they do not include other dark structure, clumped in filaments and absent in voids. This missing matter will affect the overall density of the universe so it is necessary to take this into account when estimating  $\kappa$  and  $\mu$ . We account for this by subtracting

<sup>2</sup> <http://github.com/drphilmarshall/Pangloss>



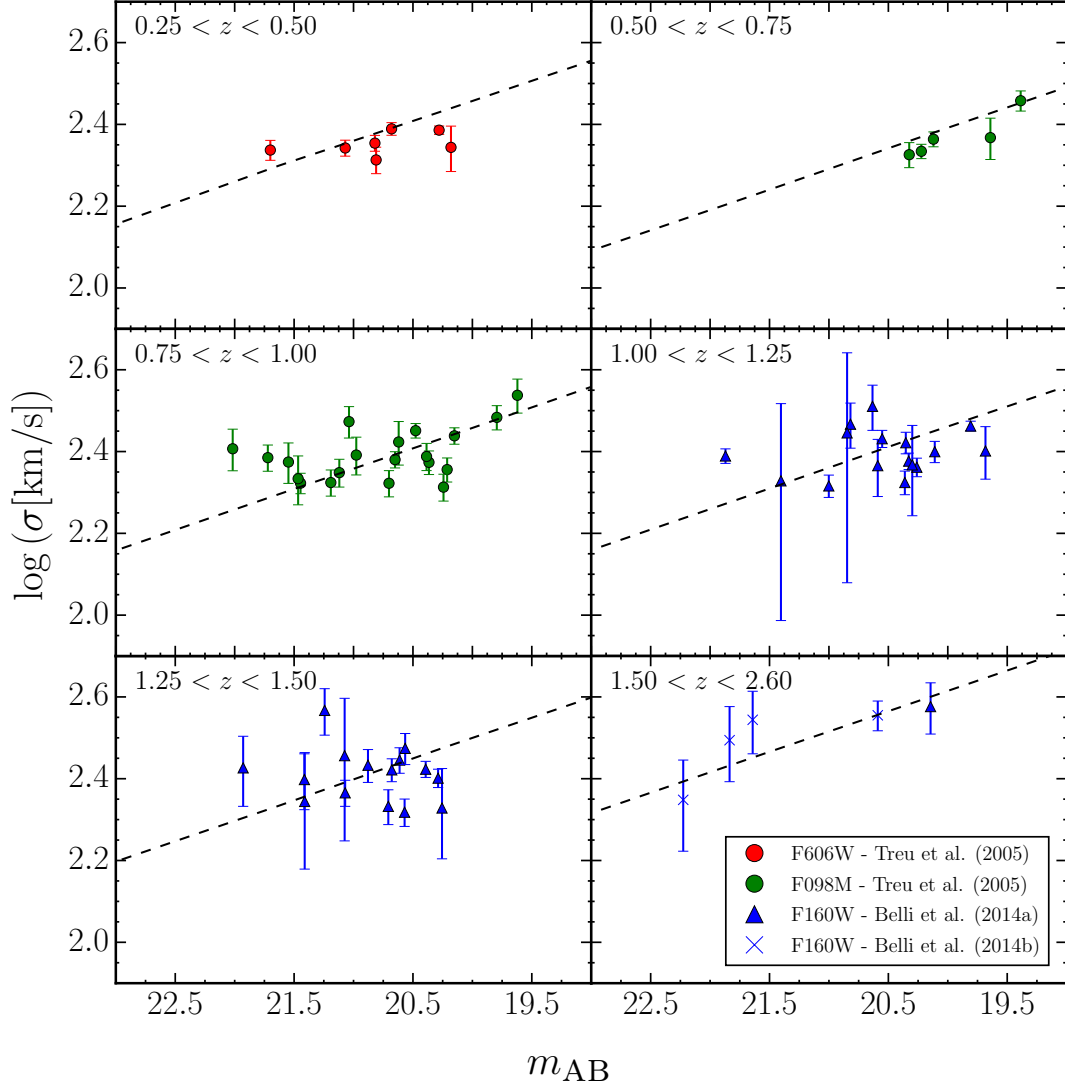


FIG. 5.— Evolving Faber-Jackson relation for massive galaxies with redshift. Data for  $z < 1$  are from Treu et al. (2005) (red and green circles), data for  $z > 1$  are from Belli et al. (2014a) (blue triangles) and Belli et al. (2014b) (blue crosses). Red points indicate apparent magnitude in the F606W band ( $z < 0.5$ ), green points have magnitudes in the F098M band ( $0.5 < z < 1$ ), and blue points are data with magnitudes in the F160W band ( $z > 2$ ). Only galaxies with  $\sigma > 200 \text{ km s}^{-1}$  were used in the fitting. The slope of the relation in velocity dispersion and magnitude is fixed at the Faber & Jackson (1976) result of  $L \propto \sigma^4$ . We fit the evolution with redshift, which changes the intercept of the line on the velocity dispersion axis. The black dashed lines shows the mean fit for the mean redshift of objects in each plotted bin. The fitting parameters are given in Table 1.

TABLE 2  
STRONG AND INTERMEDIATE LENSING PARAMETERS DERIVED BY ESTIMATING VELOCITY DISPERSIONS OF BRIGHT FOREGROUND GALAXIES CLOSE TO  $z \sim 8$  DROPOUTS

Field	Dropout ID	$J_{125}^a$	Foreground ID	$z_f$	Separation (")	$\sigma_{\text{inf}} (\text{km s}^{-1})$	$\theta_{\text{ER}} (")$	$\mu$
borg_0436-5259	1233 <sup>b,c</sup>	$27.1 \pm 0.2$	1191	1.52	2.79	$294 \pm 47$	$1.32 \pm 0.40$	$2.05 \pm 0.52$
borg_1301+0000	160 <sup>d</sup>	$25.5 \pm 0.2$	144	1.14	1.99	$184 \pm 31$	$0.60 \pm 0.20$	$1.47 \pm 0.30$
borg_1408+5503	980 <sup>c</sup>	$27.0 \pm 0.2$	959	0.40	3.11	$193 \pm 69$	$1.01 \pm 0.70$	$1.54 \pm 0.62$
borg_2155-4411	341 <sup>c</sup>	$26.6 \pm 0.2$	244	0.74	2.27	$216 \pm 22$	$0.97 \pm 0.20$	$1.80 \pm 0.33$

NOTE. — <sup>a</sup> Total (AUTOMAG) apparent magnitude in the J-band of the dropout (Bradley et al. 2012).

<sup>b</sup> Strongly-lensed candidate. <sup>c</sup>  $5\sigma$  source. <sup>d</sup>  $8\sigma$  source.

convergence from redshift slices so that the mean convergence along all lines-of-sight in the catalogs to a given redshift equals zero, and the mean magnification is unity, as they should be.

Following work by Suyu et al. (2010) and Greene et al. (2013), we compare lines-of-sight in the BoRG fields with

simulation data based on relative density of objects. We define the overdensity parameter

$$\xi = \frac{n_i}{n_{\text{tot}}} \quad (14)$$

where  $n_i$  is the number of objects per unit area in each

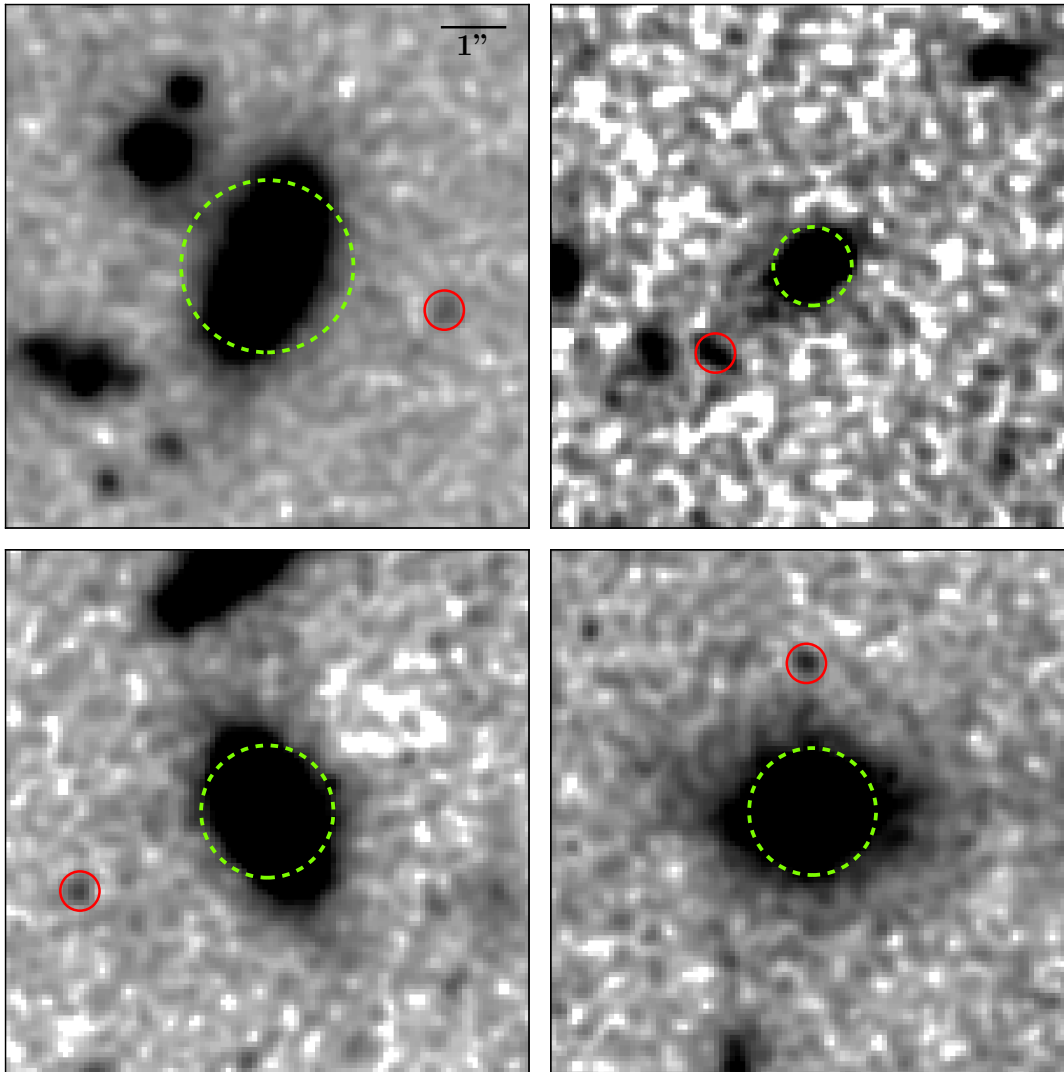


FIG. 6.— The four BoRG dropouts (from top left to bottom right: borg\_0436-5259.1233, borg\_1301+0000.160, borg\_1408+5503 and borg\_2155-4411.341) with significant magnification probabilities, shown in the F125W band with a Gaussian smoothing radius of 1 in  $8''$  boxes. The solid red lines outline the dropouts with a  $0.3''$  radius. The dashed green lines outline the potential foreground deflectors, with radius corresponding to the Einstein radius of an SIS deflector lensing a source at  $z = 8$ . The candidate strong lens system (borg\_0436-5259.1233) is shown in the top left panel, and has an estimated magnification of  $\mu = 2.05 \pm 0.52$ . Interestingly, borg\_1301+0000.160 (top right) is the brightest dropout in the BoRG survey. The parameters for all of these objects are given in Table 2.

lightcone (or real field) and  $n_{\text{tot}}$  is the total number of objects divided by the total survey area. Given that the simulation catalogs are  $\sim 500\times$  larger than the total BoRG survey area we expect them to give representative results.

We then calculate the number of objects per square arcsecond brighter than  $m = 24$  in the J-band in each of the BoRG fields compared to the the total number of objects above this flux limit in the whole survey. Similarly we calculate the overdensity of objects above the same limit in the simulated lightcones. Henriques et al. (2012) include mock photometry based on stellar population synthesis codes by Maraston (2005) which include J-band magnitudes. As shown in Figure 7, the distribution of overdensities for the observed data is within the range of that for simulated data. Finally, to generate magnification PDFs for a given BoRG field, we combine the magnifications from all simulation lines-of-sight which are within  $\pm 2\%$  in overdensity of the observed value.

In Figure 8 we plot the magnification PDFs for a source at various redshifts over all lines-of-sight. As the source redshift increases, the peak of the distribution shifts to lower magnification, but the high-magnification tail becomes more important, such that the mean magnification over all lines-of-sight remains unity. We match results for  $z < 6$  from Hilbert et al. (2007) well. It is clear that there is little change in the distribution between  $z_S = 6$  and  $z_S = 8$ , as there are negligible numbers of large halos above  $z > 5$ .

In Figure 9 we plot the magnification PDFs for a variety of overdensities. The more overdense lines-of-sight produce a higher mean magnification, as expected, but also have a greater variance than the distributions for underdense lines-of-sight. This agrees well with the estimates at lower redshift by Greene et al. (2013).

## 5.2. BoRG Weak Lensing Magnification PDFs

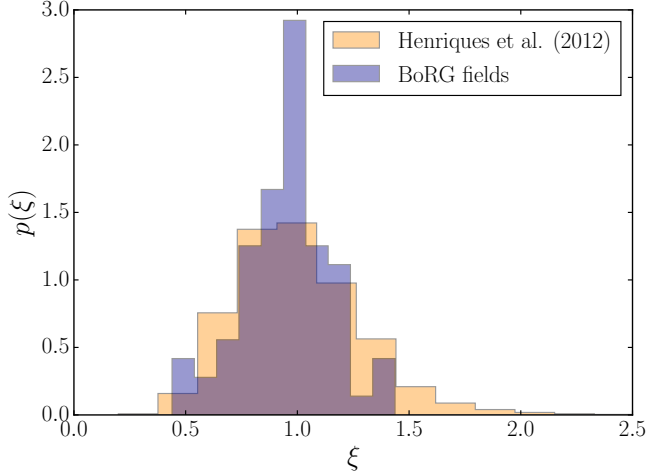


FIG. 7.— Comparison of the overdensity of lines-of-sight in the Millennium Simulation and the BoRG fields.  $\xi = n_i/n_{\text{tot}}$  where  $n_i$  is the number of objects per unit area above a certain flux limit in each lightcone (or real BoRG field) and  $n_{\text{tot}}$  is the total number of objects above the same flux limit divided by the total survey area. We use a flux limit of  $m < 24$  in F125W (J-band).

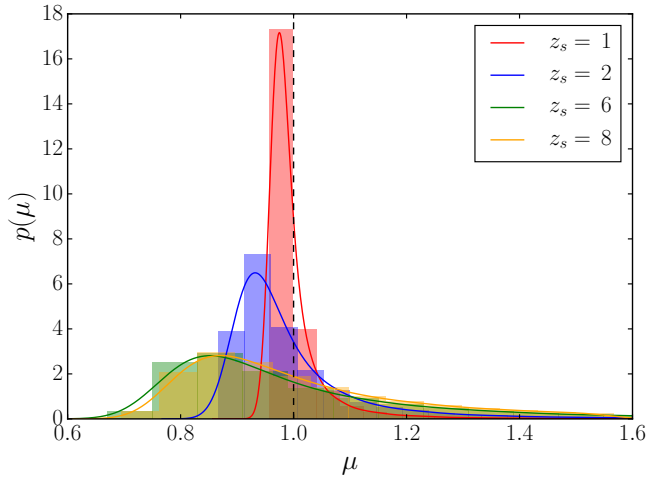


FIG. 8.— Probability distribution function for magnification for four values of source redshift. The dashed line marks the mean magnification of the universe. These results compare well with Hilbert et al. (2007). Due to the lack of significant mass between  $z \sim 6$  and  $z \sim 8$  there is little change in the distributions of magnification for sources at those redshifts, as the total convergence does not change much.

The kernel density estimates (Rosenblatt 1956; Parzen 1962) fit to the magnification PDFs for all the BoRG fields are shown in Figure 10. As expected, the BoRG fields do not have significant over- or underdensities, but are rather typical of blank fields at  $z \sim 8$ , as shown in Figure 8.

There is significant motivation for the magnification PDFs to take a log-normal form. The 3D matter density distribution of the universe is well-described by a log-normal random field (Coles & Jones 1991), and weak lensing probability distributions arise directly from the mass distribution. However, when accounting for the magnification bias in individual fields to infer the LF from the dropout sample (see Section 6) it was necessary to express the magnification distributions in a form that

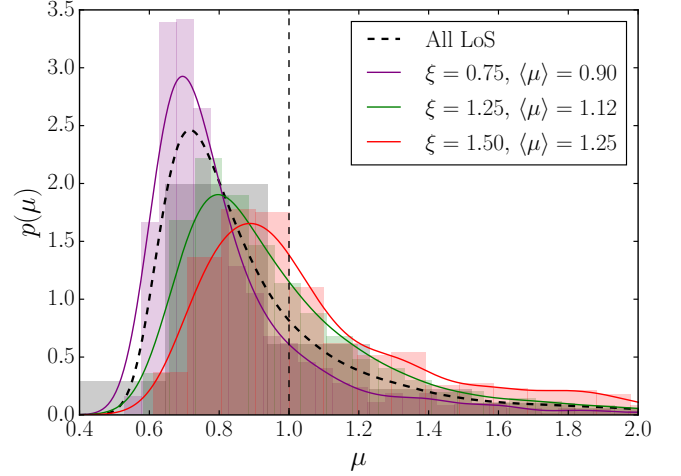


FIG. 9.— Probability distribution function for magnification for a range of values of overdensities for a source at  $z = 8$ . More overdense lines-of-sight are skewed towards higher magnification, with a broad distribution. More underdense lines-of-sight are skewed towards lower magnification, with a narrower distribution due to the deficit of intervening mass.

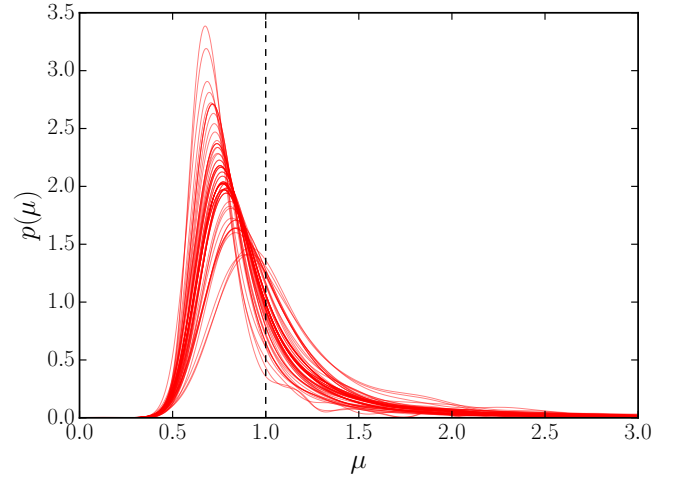


FIG. 10.— Probability distribution function for magnification for all of the BoRG fields, with a source at  $z \sim 8$ . The lines are kernel density estimations to the distributions. It is clear there is little range in overdensity for the BoRG fields.

could easily convolve analytically with a Gaussian distribution (for more details see Appendix A). For this we used a Bayesian MCMC approach to fit the distributions of magnification for each field as a linear sum of Gaussian functions.

## 6. RECOMPUTING THE LF

In this section we outline the method of estimating the  $z \sim 8$  LF from the BoRG high-redshift candidates, taking the magnification bias into account.

Following Schmidt et al. (2014a), who did not account for the magnification bias when estimating the BoRG  $z \sim 8$  LF, we use the Bayesian inference method devised by Kelly et al. (2008), which is described in Section 6.1 and in Appendix A. In Section 6.2 we describe in more detail how we take into account the weak and intermediate lensing magnification.

### 6.1. Bayesian Estimation of the LF

As in Schmidt et al. (2014a), we assume that the intrinsic luminosity function is modeled by the Schechter function in Equation (3). In order to facilitate comparison with our previous work we use the sample of 38 BoRG Y-band dropouts and 59 additional fainter dropouts from the Hubble Ultra-Deep Field (HUDF) and Early Release Science (ERS) programs (Bouwens et al. 2011).

Bayesian statistics allows us to express the posterior probability that the LF is fit by a Schechter function with parameters  $\theta = (\alpha, L^*, \Psi^*)$  given the observed luminosity  $L_{J,\text{obs}}$  of the dropouts in the J-band, and the non-detections in the V-band ( $I_V = 0$ ), as the product of the prior on the Schechter parameters and the likelihood:

$$p(\theta | L_{J,\text{obs}}, I_V = 0) \propto p(\theta) \times p(L_{J,\text{obs}}, I_V = 0 | \theta) \quad (15)$$

This posterior probability can be expressed (see Appendix A for full details) as:

$$\begin{aligned} p(\theta | L_{J,\text{obs}}, I_V = 0) &\propto p(\theta) \times C_{(1-f)n}^{N_z} \times C_{fn}^{\frac{f}{1-f}N_z} \\ &\times \prod_l^C \left[ 1 - \frac{A_l}{\bar{\mu}_l A_{\text{sky}}} p(I = 1 | \theta) \right]^{\frac{N_z - (1-f_l)c_l}{1-f_l}} \\ &\times \prod_i^n p(L_{J,\text{obs},i} | \theta) \end{aligned} \quad (16)$$

Where we iterate over  $l$  fields with  $i$   $z \sim 8$  candidates. Here  $N_z$  is the number of high- $z$  dropouts in the surveyed comoving cosmological volume,  $A_l$  is the area of the individual  $C$  fields in Schmidt et al. (2014a), which each contain  $c_l$  high redshift candidates ( $n = \sum_l^C c_l$ ). Each candidate has an assumed contamination fraction of  $f_l$ . We use a fiducial value for the contamination of 42% following Schmidt et al. (2014a) and Bradley et al. (2012).  $A_{\text{sky}}$  is the area of the full sky. The  $C_b^a$  factors are binomial coefficients which are the fully correct method of modeling source counts.

We assume uniform priors on  $\alpha$ ,  $\log_{10} L^*$  and  $\log_{10} N_z$ .  $p(I = 1 | \theta)$  is the probability distribution of an object making it into the dropout sample based on the photometric selection described in Schmidt et al. (2014a).  $p(L_{J,\text{obs},i} | \theta)$  is the likelihood function for the observed J-band luminosity of the  $i$ 'th object in the sample.

The last term includes marginalization over the magnification PDF:

$$\begin{aligned} p(L_{J,\text{obs}} | \theta) &= \int \int p(\mu) p(L_{J,\text{obs}} | \mu L_{J,\text{true}}) \\ &\times p(L_{J,\text{true}} | \theta) dL_{J,\text{true}} d\mu \end{aligned} \quad (17)$$

In Appendix A we give the expanded expression of the posterior distribution from Equation (16) used when performing the LF parameter inference and describe the derivation and motivation for Equation (17). We refer to Appendix A and Schmidt et al. (2014a) for further details.

### 6.2. Including the Lensing Corrections

#### 6.2.1. Analytic Form for Magnification PDFs

In order to make integration of Equation (17) computationally feasible we require a simple analytic form for

$p(\mu)$  that will convolve simply with a Gaussian distribution (see Appendix A). As described in Section 5.2, the weak lensing magnification PDF is well-fit by a log-normal distribution. However, this cannot be convolved analytically with a Gaussian.

Therefore, we fit the magnification PDFs from all regimes as a linear combination of Gaussian functions with different means and standard deviations. The weak lensing magnification PDFs (see Section 5.2) are well-fit by a combination of three Gaussian functions. The intermediate lensing PDFs (see Section 4.2) are also well-fit by a combination of three Gaussian functions.

#### 6.2.2. Combining Lensing Regimes

All of the fields have a weak lensing magnification PDFs based on their overdensity (see Section 5), but we have also identified one strongly-lensed candidate and three dropouts close to large foreground galaxies that produce an intermediate magnification PDF (see Section 4.2).

To account for the magnification bias, we need to use the correct magnification PDF for each field. In the case when a strong or intermediate lens appears present, we split the field into two parts for the calculation of the posterior: one is a circle with radius  $10 \theta_{\text{ER}}$  containing the dropout and the deflector, where we use the strong or intermediate lens magnification PDF. For the remainder of the field we use the weak lensing magnification PDF.

Whilst the total flux across the sky is conserved, locally over- or underdensities that produce magnification not only magnify fluxes, but also increases areas. Hence, the individual BoRG fields we observe have been magnified (or demagnified) from their true sizes. We account for this in the posterior probability Equation (16) by dividing the measured area of each field by the mean magnification in that field,  $\bar{\mu}_l$  from the magnification PDFs. For weak lensing magnification PDFs  $\langle \mu_l \rangle \sim 1$ . For the intermediate lensing case  $1.4 < \bar{\mu}_l < 2$  due to our selection process.

As magnification is most important for the bright-end of the LF, and negligible at the faint end, for simplicity and without loss of precision, we adopt  $\mu = 1$  for the 59 fainter dropouts (Bouwens et al. 2011). Additionally, one of the BoRG fields (borg\_1815.3244) is centered on the Galactic plane and is dominated by stars. We discard this field in our calculation of the LF.

## 7. RESULTS

Using the framework described in Section 6 to account for the magnification bias we present our estimation of the  $z \sim 8$  galaxy LF based on our sample of 97  $z \sim 8$  LBGs (described in Section 2). First, in Section 7.1 we compare our estimates of strong and intermediate lensing probabilities with the actual observations. Then, in Section 7.2 we carry out the inference of the  $z \sim 8$  LF. Finally, in Section 7.3, we use our semi-analytical model of strong lensing optical depths described in Section 4 to predict the form of observed LFs at  $z \geq 8$ .

### 7.1. Strong and Intermediate Lensing Events in the BoRG Survey

The simple SIS strong lensing model described in Section 4.1 predicts the probability of  $z \sim 8$  sources in the



BoRG survey being multiply imaged to be  $\sim 3-15\%$ , increasing as the field limiting magnitude becomes brighter than  $M^*$ . The majority of the BoRG fields have a multiple-image probability for high-redshift sources of  $< 10\%$  (see Figure 4). We predict that 1-2 of the 38 BoRG Y-band dropouts may be strongly lensed.

One candidate strong lens system in BoRG was presented by Barone-Nugent et al. (2013), a rigorous search for strong lenses in all 71 BoRG fields as part of this work revealed one more candidate. Additionally, this search revealed three candidate intermediate lens systems, with  $\mu > 1.4$ . These candidates are presented in Figure 6 and Table 2. Whilst strong lensing creates larger magnification, the probability of encountering a strong lens along the line-of-sight is low: as shown in Figure 3 the optical depth is roughly  $\tau \approx 0.35\%$  for a source at  $z = 8$ . The optical depth for intermediate lensing is much higher: for an object to experience intermediate lensing it must be within  $3.5\theta_{\text{ER}}$  of the foreground deflector, resulting in  $\tau \approx 4\%$  for a source at  $z = 8$ . Thus, intermediate lensing offers an additional boost to the flux of high-redshift galaxies, and must be correctly accounted for in estimations of the LF.

### 7.2. Inference of the Intrinsic $z \sim 8$ LF

We estimate the  $z \sim 8$  LF from the sample of 97 LBG described in Section 2, including the 38  $S/N_J > 5$  objects from the BoRG survey, including the effects of magnification bias. We sample the posterior distribution function for the Schechter function parameters with an MCMC chain of 40 000 steps.

The results of the estimated LF are shown in Figure 11, and the correlations between the Schechter function parameters and their PDFs are shown in Figure 12. We plot the results of Schmidt et al. (2014a) for comparison in both figures. We see a small deviation from the uncorrected LF of  $\sim 0.15$  mag at the limit of the brightest BoRG source, and there is negligible difference between the LFs at  $M > -21$ . The Schechter function parameters for the new LF are within the uncertainties of the estimation by Schmidt et al. (2014a), though we find a slightly fainter value of  $M^*$  and higher value of  $\Psi^*$  than Schmidt et al. (2014a). This is expected because of the slight deviation at the bright end of the LF, and there is a strong correlation between these parameters, as shown in Figure 12. It is clear that magnification bias is not a significant effect at this redshift and the luminosity range of the BoRG sources.

Table 3 summarizes the estimated Schechter function parameters for this LF in comparison with other recent LF estimates from the literature. We find that our fit parameters are in good agreement with the recent literature, demonstrating that magnification bias is not affecting current  $z \sim 8$  LF observations. Note that our results have significantly smaller error bars than those of Finkelstein et al. (2014), because their sample contains only 3  $z \sim 8$  galaxies brighter than  $M = -21$ , making their fit less well-constrained at the bright end.

Our results show that magnification bias does not affect current estimates of the LF at  $z \lesssim 8$  and therefore cannot explain the apparent flattening of the bright-end of the LF recently observed by Bowler et al. (2014a,b) and Finkelstein et al. (2014) at  $z \sim 7-8$ . Bowler et al. (2014a,b) accounted for strong lensing of bright

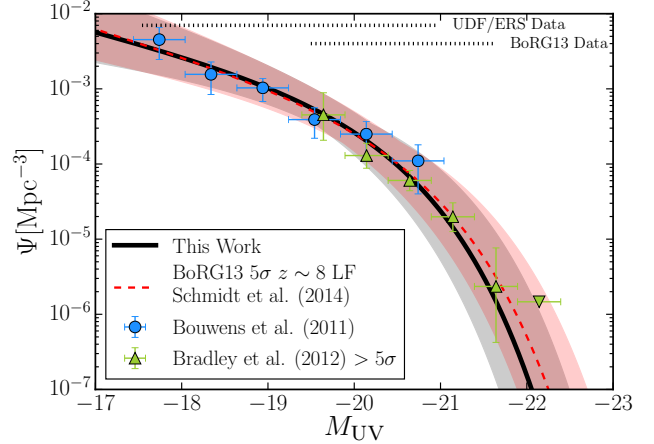


FIG. 11.— The intrinsic  $z \sim 8$  LF, which is well-described by a Schechter (1976) function, including the magnification bias due to weak and intermediate lensing in all BoRG fields (solid black line). We plot the LF without the treatment of the magnification bias (Schmidt et al. 2014a) for comparison (dashed red line). The lines corresponds to the median values of the MCMC samples and the shaded regions correspond to the 68% confidence region of the samples. The LF estimated here is virtually indistinguishable from that of Schmidt et al. (2014a), demonstrating that magnification bias is not a significant effect at  $z \sim 8$ . The Schechter parameters for this LF are given in Table 3 along with literature values. The binned data from BoRG12 (Bradley et al. 2012) and the faint HUDF/ERS candidates (Bouwens et al. 2011) are also plotted as blue and green points respectively. The inverted green triangle denotes the brightest BoRG dropout. We note that the LF is estimated from the unbinned data.

sources, but they still find a deviation of  $\sim 0.4$  mag from a Schechter fit at  $M = -22$ . We predict a lensed fraction of  $\sim 3-15\%$  for bright galaxies (Figure 4) from the BoRG survey which is essentially free of cosmic variance (Trenti & Stiavelli 2008), so providing cosmic variance was correctly accounted for the work of Bowler et al. (2014a,b) and Finkelstein et al. (2014), we expect the magnification bias to be negligible in the bright-end of these LFs. This lends credence to the interpretation that these observations may be the result of the changing intrinsic properties of galaxies at  $z \gtrsim 7$ , possibly due to changing dust fractions (Cai et al. 2014) and/or feedback processes (Somerville et al. 2012).

### 7.3. Predictions for $z > 8$ and Future Surveys

There is clear evolution in the LF for  $z < 8$  (e.g. Bouwens et al. 2007; van der Burg et al. 2010; Bouwens et al. 2014; Bowler et al. 2014a; Finkelstein et al. 2014), and this is expected to continue to higher redshifts. However, the processes which drive this evolution are not well-understood: the evolution is thought to follow hierarchical structure formation and the evolution of the halo mass function (Vale & Ostriker 2004), but there are also important quenching processes that may reduce star formation in massive galaxies (Schneider et al. 2006; Somerville et al. 2012), and changes in the amount of dust present in galaxies will affect the attenuation of flux. Thus there are a multitude of theoretical models for the evolution of the LF.

The gravitationally lensed LF (Equation (10)) exhibits a significant ‘kick’ in the bright-end tail for  $M \lesssim -22$  at  $z \sim 8$ . This is just beyond the brightest BoRG objects, so

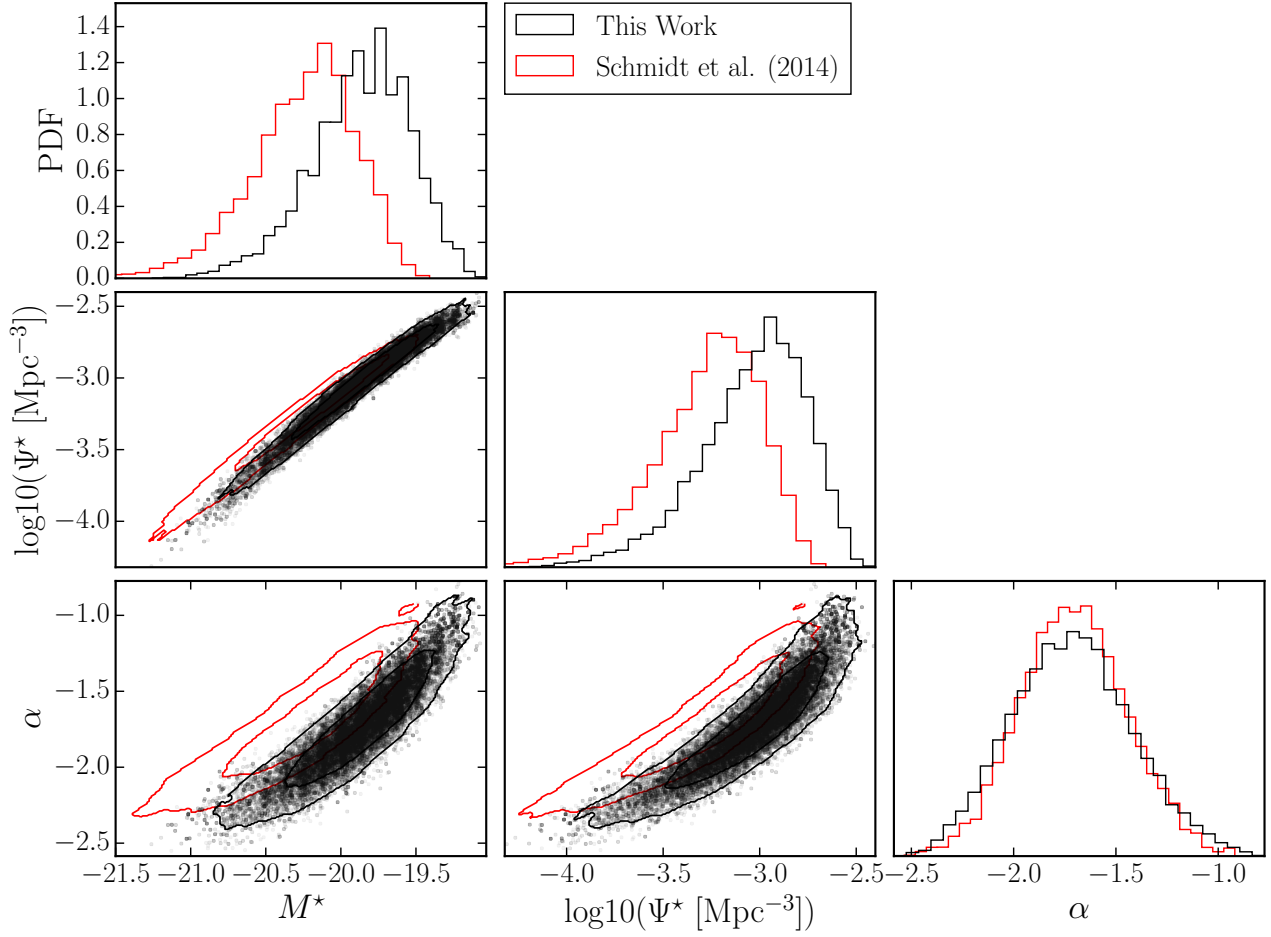


FIG. 12.— The correlations between the  $z \sim 8$  LF Schechter function parameters ( $\alpha$ ,  $M^*$  and  $\Psi^*$ ) estimated from the BoRG dropouts including treatment of magnification bias (black), compared to the parameters obtained without the treatment of magnification bias (red, Schmidt et al. 2014a) with  $1\sigma$  and  $2\sigma$  confidence contours. There is clear correlation between all three parameters. The top panels show the marginalised PDFs for each parameter.

TABLE 3  
COMPARISON OF  $z \sim 8$  SCHECHTER LF PARAMETERS

Reference	$M^*$	$\alpha$	$\log_{10} \Psi^* [\text{Mpc}^{-3}]$
This work	$-19.85^{+0.30}_{-0.35}$	$-1.72^{+0.30}_{-0.29}$	$-3.00^{+0.23}_{-0.31}$
Finkelstein et al. (2014)	$-20.89^{+0.74}_{-1.08}$	$-2.36^{+0.54}_{-0.40}$	$-4.14^{+0.65}_{-1.01}$
Bouwens et al. (2014)	$-19.97 \pm 0.34$	$-1.86 \pm 0.27$	$-3.19 \pm 0.30$
Schmidt et al. (2014a) $5\sigma$	$-20.15^{+0.29}_{-0.38}$	$-1.87^{+0.26}_{-0.26}$	$-3.24^{+0.25}_{-0.34}$
Schmidt et al. (2014a) $8\sigma$	$-20.40^{+0.39}_{-0.55}$	$-2.08^{+0.30}_{-0.29}$	$-3.51^{+0.36}_{-0.52}$
Bradley et al. (2012)	$-20.26^{+0.29}_{-0.34}$	$-1.98^{+0.23}_{-0.22}$	$-3.37^{+0.26}_{-0.29}$
Oesch et al. (2012)	$-19.80^{+0.46}_{-0.57}$	$-2.06^{+0.45}_{-0.37}$	$-3.17^{+0.40}_{-0.55}$
Bouwens et al. (2011)	$-20.10 \pm 0.52$	$-1.91 \pm 0.32$	$-3.23^{+0.74}_{-0.27}$

it is unlikely that the BoRG survey observes the regime of magnification bias at the bright-end. However, in upcoming wide-area surveys magnification bias presents a useful tool to test LF evolution models because it allows us to probe the bright end, where there are large theoretical uncertainties and the evolution is expected to be fast (Bowler et al. 2014a).

In order to explore the range of possible scenarios, in Figure 13 we plot the predicted intrinsic (dashed lines) and observed (solid lines) LFs for a range of redshifts,

comparing a variety of evolution models. We assume these models are the intrinsic LFs at a given redshift and used Equation (10) to estimate the observed LF. We plot the BoRG  $z \sim 8$  LF (Schmidt et al. 2014a) for comparison. Additionally, we mark the comoving volumes and magnitude ranges accessible to future high-redshift surveys.

The top left panel shows the LF model from Bouwens et al. (2014) which is an extrapolation from observations at  $z < 10$ . The top right panel shows the LF model from

Finkelstein et al. (2014) which is an extrapolation from observations at  $4 < z < 8$ . The bottom left panel shows the model developed by Muñoz (2012) which follows the evolution of the halo mass function, and includes dust attenuation. The bottom right panel is a model from Behroozi et al. (in preparation) constructed from a comparison of the specific star formation rate to the specific halo mass accretion rate, and including dust models from Charlot & Fall (2000). The Finkelstein et al. (2014) model predicts a slower evolution than the others, probably because they found a negligible evolution in  $M^*$  compared to Bouwens et al. (2014). The four models have significantly different behaviors at the bright end. While the Bouwens et al. (2014) model has by construction a bright end that is very similar to that measured at lower redshifts, the Muñoz (2012) model has a very shallow bright end, and the (Finkelstein et al. 2014) and Behroozi et al. models are inbetween. As a result, the effects of magnification bias (which are stronger for the steeper LF) are very different: negligible in the Muñoz (2012) case and appreciable in the three other cases. However, the bright end of the Muñoz (2012) model is the easier one to test observationally, within reach of a James Webb Space Telescope medium depth, medium width survey (e.g. JWST MD Windhorst et al. 2006).

Except in the case of a very shallow bright end, we do not expect the magnification bias to be significant in our upcoming BoRG  $z \sim 9, 10$  survey (HST Cycle 22, PI Trenti). In all cases, it is clear that surveys covering  $> 100 \text{ deg}^2$ , e.g. Euclid and WFIRST, should find many bright  $z > 8$  LBGs. We expect the observed high-redshift galaxy samples will be dominated by magnification bias in these surveys. We predict almost all  $z \sim 8$  sources in Euclid will have been strongly lensed. The framework developed in this work will be vital for determining the intrinsic luminosity of high-redshift sources found in such surveys.

Our results confirm the suggestion by Wyithe et al. (2011) that magnification bias will be important to probe the bright end of the LF at high redshift. However, we find that the magnitude of the effect is less pronounced than in that study, owing mostly to our accounting for the redshift evolution of the deflector population.

## 8. SUMMARY AND CONCLUSION

We have introduced a systematic way to account for the magnification bias in estimations of high-redshift LFs. The method involves estimating the probability density function for weak lensing magnification along a given line-of-sight by comparison with results from the reconstruction of simulated halo data, and by estimating the strong and intermediate lensing magnification PDF of dropouts due to massive deflector galaxies in close proximity to the dropout.

We applied this method to estimate the  $z \sim 8$  LF from the 38 BoRG Y-band dropouts and 59 fainter dropouts from Bouwens et al. (2011). Our main results are summarized as follows:

- (a) The probability of a BoRG  $z \sim 8$  dropout being multiply imaged is  $\sim 3 - 15\%$ , increasing with limiting magnitude. This is consistent with finding two

strongly-lensed dropouts in the BoRG survey: the candidate system presented in Barone-Nugent et al. (2013), and the additional strongly-lensed candidate dropout in this paper. We also find three dropouts which may experience significant magnification without multiple imaging, consistent with our expectations.

- (b) We extended the Bayesian formalism for the estimation of the LF parameters presented by Schmidt et al. (2014a) to account for the magnification bias. This involves marginalizing over the magnification PDFs for strong and weak lensing effects. The inferred Schechter function parameters are:

$$\begin{aligned} M^* &= -19.85^{+0.30}_{-0.35}, \\ \alpha &= -1.72^{+0.30}_{-0.29}, \\ \log_{10} \Psi^* [\text{Mpc}^{-3}] &= -3.00^{+0.23}_{-0.31}, \end{aligned}$$

These values do not differ significantly from estimates not accounting for the magnification bias.

- (c) Thus magnification bias cannot be an explanation for the apparent flattening of the bright-end of the LF recently observed by Bowler et al. (2014a,b) and Finkelstein et al. (2014), suggesting these observations may be due to the changing properties of galaxies at  $z \gtrsim 7$ .
- (d) The  $z \sim 8$  LF appears significantly magnified for extremely bright galaxies ( $M_{\text{UV}} < -22$ ). Though current surveys have not observed such rare, luminous galaxies, future wide-field surveys will probe this region. For surveys  $> 100 \text{ deg}^2$ , e.g. WFIRST, Euclid, we predict that samples of  $z \gtrsim 8$  galaxies will be dominated by magnification bias.
- (e) Magnification bias will be a useful tool to distinguish between high-redshift LF evolution models. In particular it could help determine whether the LF transitions from a Schechter form to a power-law form at high redshift, indicating significant changes in the astrophysical properties of those galaxies.

We thank Joey Muñoz for useful discussions and providing his LF evolution model; Peter Behroozi for providing his LF evolution model; Sirio Belli for providing photometry of the galaxies described in Belli et al. (2014a,b); and Stefan Hilbert for useful comments regarding the weak lensing simulations.

This work was supported by the HST BoRG grants GO-11700, 12572, and 12905. This paper is based on observations made with the NASA/ESA Hubble Space Telescope, obtained at the Space Telescope Science Institute.

This work made use of the freely available Pangloss code, written by Tom Collett and Phil Marshall. The Millennium Simulation databases used in this paper are publicly available through the German Astrophysical Virtual Observatory.

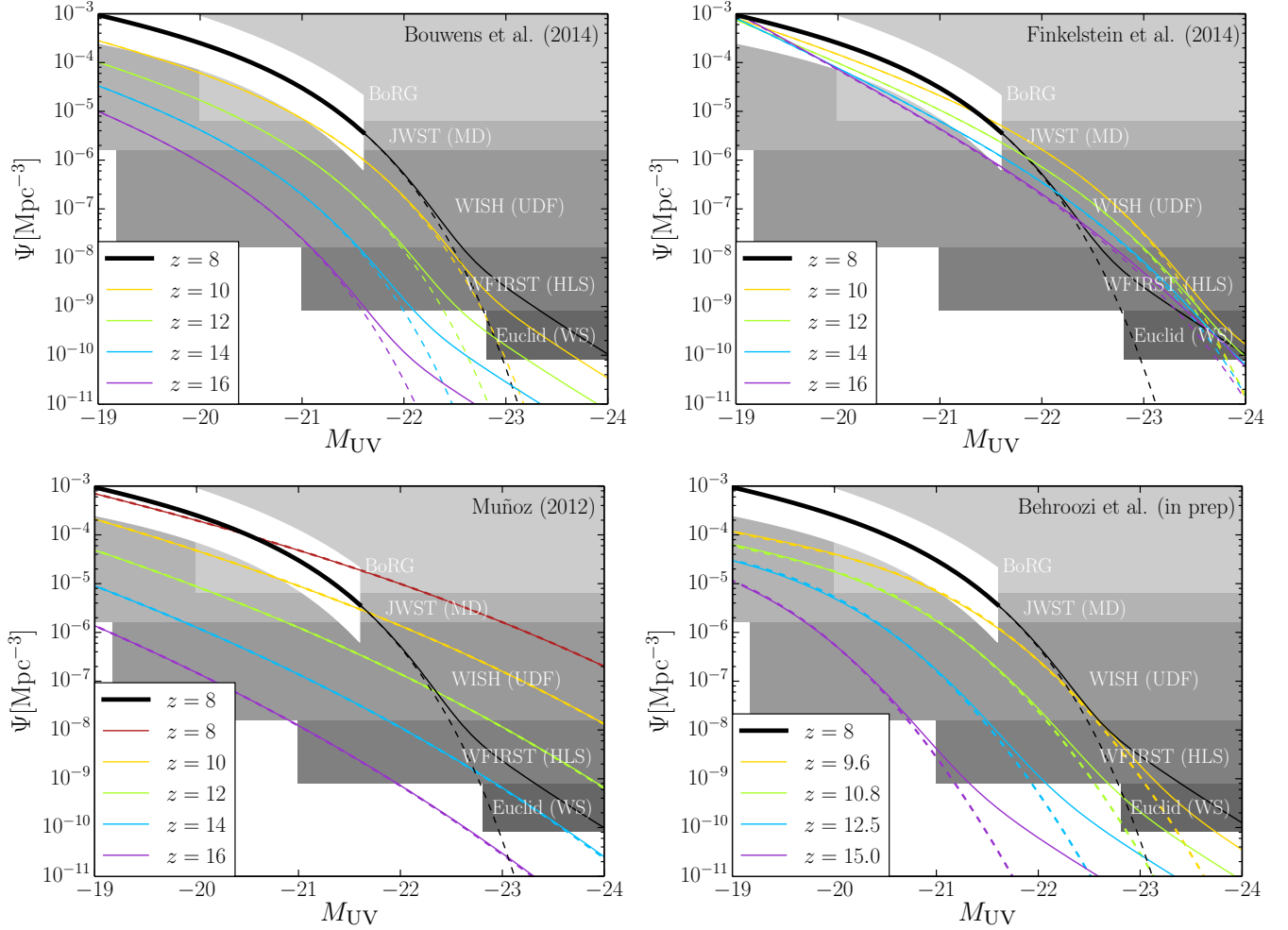


FIG. 13.— Predicted observed LFs for  $z \geq 8$  redshifts. For  $z = 8$  we use the Schechter LF from Schmidt et al. (2014a), plotted as a thick black line. The white band indicates the error on the Schechter function parameters, and the thin black line is the extrapolation of the LF beyond the observational limit. We show the regions of magnitude and volume observable by current and future surveys: the total BoRG survey including the  $z \sim 8$  survey described in Section 2.1 and the upcoming BoRG  $z \sim 9, 10$  survey (HST Cycle 22, PI: Trenti); the James Webb Telescope Medium Deep (JWST MD) (Windhorst et al. 2006); the Wide-Field Imaging Surveyor for High-Redshift Ultra-Deep Field (WISH UDF, <http://wishmission.org/en/doc.html>); the Wide-Field Infrared Survey Telescope High Latitude Survey (WFIRST HLS) (Spergel et al. 2013) and the Euclid Wide Survey (WS) (Laureijs et al. 2011). As explained in the text, BoRG does not survey enough area to observe the rarest bright sources which are most affected by magnification bias, but future wide-field surveys will be dominated by this effect. **(Top Left)** For  $z > 8$  we use the LF model from Bouwens et al. (2014) which is an extrapolation from  $z \sim 10$ . **(Top Right)** For  $z > 8$  we use extrapolate the evolution of the Schechter function parameters over  $4 < z < 8$  from Finkelstein et al. (2014). **(Bottom Left)** For  $z \geq 8$  we use the luminosity model from Muñoz (2012) which is based on the evolution of the halo mass function. These do not exhibit the sharp cut-off at the bright-end and are not affected by magnification bias. **(Bottom Right)** For  $z > 8$  we use the LF evolution model from Behroozi et al. (in preparation). The dashed lines indicate the intrinsic LFs, the solid lines are the observed LFs including the magnification bias calculated using Equation (10).



## APPENDIX

## A. BAYESIAN FRAMEWORK FOR ESTIMATING THE LUMINOSITY FUNCTION

We use Bayesian statistics to find the relationship between the prior probability of the  $z \sim 8$  dropouts being galaxies with LF Schechter parameters  $\theta = (\alpha, L^*, \Psi^*)$ , and these parameters' posterior probability given the dropout candidates' detection threshold in the J-band, assuming their non-detection in the V-band. The posterior probability is given by:

$$p(\theta | L_{J,\text{obs}}, I_V = 0) \propto p(\theta) \times p(L_{J,\text{obs}}, I_V = 0 | \theta) \quad (\text{A1})$$

where the last term is the likelihood and  $p(\theta)$  is the prior on the LF parameters. We will assume uniform priors on  $\alpha$  and  $\log_{10} L^*$ .

We can expand the expression for the posterior:

$$\begin{aligned} p(\theta | L_{J,\text{obs}}, I_V = 0) \propto & p(\theta) C_{n_z}^{N_z} \prod_l^C [1 - A_l/A_{\text{sky}} p(I = 1|\theta)]^{N_z - c_{lz}} \times \prod_i^{n_z} p(L_{J,\text{obs},i} | \theta) \\ & \times C_{n_c}^{N_c} \prod_l^C [1 - A_l/A_{\text{sky}} p(I = 1|\theta)]^{N_c - c_{lc}} \times \prod_i^{n_c} p(L_{J,\text{obs},i} | \theta) \end{aligned} \quad (\text{A2})$$

where the  $C_b^a$  terms are binomial coefficients which correctly model the distribution of source counts.  $N_z$  and  $N_c$  are the number of high-redshift sources given the intrinsic LF and the number of potential contaminants in the Universe respectively. We will assume a uniform prior on  $\log_{10} N_z$ . In the observed sample the number of high-redshift sources and contaminants are given by  $n_z$  and  $n_c$ . The total number of galaxies in the observed sample,  $n_t$  is given by their sum. We take the product over  $C$  individual observed fields where  $c_l$  represents the number of galaxies in the  $l$ 'th field with  $n_t$  also given by the sum of  $c_l$  over all of the fields. The fraction of the sky covered by the  $l$ 'th field is given by  $A_l/A_{\text{sky}}$ . The contamination fraction in each field,  $f_l$  is set at the fiducial value of 42% (Schmidt et al. 2014a; Bradley et al. 2012).

The last term in Equation (A2) is the likelihood for the  $i$ 'th object in the sample. In Schmidt et al. (2014a) this was expressed as:

$$\begin{aligned} p(L_{J,\text{obs}} | \theta) &= \int_0^\infty p(L_{J,\text{obs}} | L_{J,\text{true}}) p(L_{J,\text{true}} | \theta) dL_{J,\text{true}} \\ &= \int_0^\infty \mathcal{N}(L_{J,\text{obs}} | L_{J,\text{true}}, \delta L_{J,\text{field}}) \text{gamma}(L_{J,\text{true}} | \alpha, L^*) dL_{J,\text{true}} \end{aligned} \quad (\text{A3})$$

where we use  $p(L | \theta) \propto \frac{\Psi(L, \theta)}{\Psi^*}$  (see Equation (1) of Kelly et al. (2008)). The function  $\text{gamma}(L_{J,\text{true}} | \alpha, L^*)$  is related to the Schechter LF (Equation (3)) as  $\text{gamma}(L | \alpha, L^*) = \frac{\Psi(L)}{\Psi^* \Gamma(\alpha+1)}$ .

$$\mathcal{N}'(L_{J,\text{obs}} | L_{J,\text{true}}, \delta L_{J,\text{field}}) = \frac{1}{\delta L_{J,\text{field}} \sqrt{2\pi}} \exp \left[ -\frac{(L_{J,\text{obs}} - L_{J,\text{true}})^2}{2 \delta L_{J,\text{field}}^2} \right] \quad (\text{A4})$$

represents the true luminosity inferred from the observations assuming a Gaussian measurement error with  $\delta L_{J,\text{field}}$  being the median photometric error in the J-band in the given field.

In order to include the effects of the magnification bias, we must integrate over the nuisance parameter  $L_{J,\text{mag}}$ , which represents the luminosity of an object in the J-band, magnified above its true luminosity. Including this Equation (A3) becomes:

$$p(L_{J,\text{obs}} | \theta) = \int \int p(L_{J,\text{obs}} | L_{J,\text{mag}}) p(L_{J,\text{mag}} | L_{J,\text{true}}) p(L_{J,\text{true}} | \theta) dL_{J,\text{true}} dL_{J,\text{mag}} \quad (\text{A5})$$

where  $p(L_{J,\text{obs}} | L_{J,\text{mag}})$  is now the term with Gaussian measurement errors similar to Equation (A4), given that we make observations of magnified luminosities:

$$\mathcal{N}(L_{J,\text{obs}} | L_{J,\text{mag}}, \delta L_{J,\text{field}}) = \frac{1}{\delta L_{J,\text{field}} \sqrt{2\pi}} \exp \left[ -\frac{(L_{J,\text{obs}} - L_{J,\text{mag}})^2}{2 \delta L_{J,\text{field}}^2} \right] \quad (\text{A6})$$

To find the probability that luminosity is magnified from its true luminosity,  $p(L_{J,\text{mag}} | L_{J,\text{true}})$ , we must integrate over the full magnification probability density:

$$p(L_{J,\text{mag}} | L_{J,\text{true}}) = \int p(L_{J,\text{mag}} | \mu, L_{J,\text{true}}) p(\mu) d\mu \quad (\text{A7})$$

We can marginalize over  $L_{J,\text{mag}}$  in the first part of Equation (A5):

$$\begin{aligned}
p(L_{J,\text{obs}} | L_{J,\text{true}}) &= \int p(L_{J,\text{obs}} | L_{J,\text{mag}}) p(L_{J,\text{mag}} | L_{J,\text{true}}) dL_{J,\text{mag}} \\
&= \int \int p(L_{J,\text{mag}} | \mu, L_{J,\text{true}}) p(\mu) p(L_{J,\text{obs}}, L_{J,\text{mag}}, \delta L_{J,\text{field}}) d\mu dL_{J,\text{mag}} \\
&= \int \int \delta(L_{J,\text{mag}} - \mu L_{J,\text{true}}) p(\mu) \mathcal{N}(L_{J,\text{obs}} | L_{J,\text{mag}}, \delta L_{J,\text{field}}) d\mu dL_{J,\text{mag}} \\
&= \int p(\mu) \mathcal{N}(L_{J,\text{obs}} | \mu L_{J,\text{true}}, \delta L_{J,\text{field}}) d\mu \\
&= \int p(\mu) \frac{1}{\delta L_{J,\text{field}} \sqrt{2\pi}} \exp \left[ -\frac{(L_{J,\text{obs}} - \mu L_{J,\text{true}})^2}{2 \delta L_{J,\text{field}}^2} \right] d\mu
\end{aligned} \tag{A8}$$

Here we have used the Dirac delta function  $\delta(L_{J,\text{mag}} - \mu L_{J,\text{true}})$  to map true luminosities to magnified luminosities. To make computation of Equation (A2) feasible, we integrate Equation (A8) analytically and want to remove any  $L_{J,\text{mag}}$  dependence we fit the magnification PDFs as a normalized linear combination of Gaussian terms with coefficients  $\beta_i$  centered on  $\bar{\mu}_{i,\text{mag}}$  with standard deviation  $\sigma_{i,\text{mag}}$ :

$$p(\mu) = \sum_i^n \beta_i \frac{1}{\sigma_{i,\text{mag}} \sqrt{2\pi}} \exp \left[ -\frac{(\mu - \bar{\mu}_{i,\text{mag}})^2}{2 \sigma_{i,\text{mag}}^2} \right] \tag{A9}$$

Equation (A8) can then be integrated analytically:

$$p(L_{J,\text{obs}} | L_{J,\text{true}}) = \sum_i^n \frac{\beta_i}{\sqrt{2\pi}} \frac{1}{\sqrt{\sigma_{i,\text{mag}}^2 L_{J,\text{true}}^2 + \delta L_{J,\text{field}}^2}} \exp \left[ -\frac{(L_{J,\text{obs}} - \bar{\mu}_{i,\text{mag}} L_{J,\text{true}})^2}{2 (\sigma_{i,\text{mag}}^2 L_{J,\text{true}}^2 + \delta L_{J,\text{field}}^2)} \right] \tag{A10}$$

As solid angle is also magnified in gravitational lensing we must divide the measured field area  $A_l$  by the average magnification in each field  $\bar{\mu}_l$ . If  $\bar{\mu}_l > 1$  the fields we observe appear larger than their true sizes.

We can therefore express Equation (A2) as (see Schmidt et al. (2014a) for details):

$$\begin{aligned}
p(\theta | L_{J,\text{obs}}, I_V = 0) &\propto p(\theta) \times C_{(1-f)n_t}^{N_z} C_{f n_t}^{\frac{f}{1-f} N_z} \\
&\times \prod_l^c \left[ 1 - \frac{A_l}{\bar{\mu}_l A_{\text{sky}}} \int_0^\infty \int_0^\infty dL_{J,\text{true},l} dL_{J,\text{obs},l} \mathcal{S}(L_{J,\text{obs},l}) \mathcal{F}(L_{J,\text{obs},l}, L_{J,\text{true},l}) \right]^{\frac{1}{1-f_l} (N_z - (1-f_l) c_l)} \\
&\times \prod_i^{n_t} \int_0^\infty \mathcal{F}(L_{J,\text{obs},i}, L_{J,\text{true},i}) dL_{J,\text{true},i}
\end{aligned} \tag{A11}$$

Here we have defined  $\mathcal{F}(L_{J,\text{obs}}, L_{J,\text{true}}) = p(L_{J,\text{obs}} | L_{J,\text{true}}) \text{gamma}(L_{J,\text{true}} | \alpha, L^*)$  and included the selection function  $\mathcal{S}(L_{J,\text{obs}})$ . The selection function estimates the completeness of the source selection and has been obtained for each individual BoRG field as explained in Oesch et al. (2012); Bradley et al. (2012) and Schmidt et al. (2014a).

Thus, Equation (A11) is the posterior probability distribution for a sample of  $n_t$  binomially distributed objects, assumed have an intrinsic Schechter LF of the form shown in Equation (3). The observed luminosity of each object is related to its true luminosity via a magnification PDF and an assumed Gaussian error distribution.

## REFERENCES

- Atek, H., Richard, J., Kneib, J.-P., et al. 2014, arXiv:1409.0512  
Auger, M. W., Treu, T., Bolton, A. S., et al. 2010, ApJ, 724, 511  
Baltz, E. A., Marshall, P., & Oguri, M. 2009, JCAP, 2009, 015  
Barkana, R., & Loeb, A. 2000, ApJ, 531, 613  
Barone-Nugent, R. L., Wyithe, J. S. B., Trenti, M., et al. 2013, arXiv:1303.6109  
Belli, S., Newman, A. B., & Ellis, R. S. 2014a, ApJ, 783, 117  
Belli, S., Newman, A. B., Ellis, R. S., & Konidaris, N. P. 2014b, ApJ, 788, L29  
Benitez, N., Ford, H., Bouwens, R. J., et al. 2004, ApJS, 150, 1  
Bezanson, R., Franx, M., & van Dokkum, P. 2014, arXiv:1410.5818  
Bezanson, R., van Dokkum, P., & Franx, M. 2012, ApJ, 760, 62  
Bezanson, R., van Dokkum, P. G., van de Sande, J., et al. 2013, ApJ, 779, L21  
Bezanson, R., van Dokkum, P. G., Franx, M., et al. 2011, ApJ, 737, L31  
Blaizot, J., Wadadekar, Y., Guiderdoni, B., et al. 2005, MNRAS, 360, 159  
Bouwens, R. J., Illingworth, G. D., Franx, M., & Ford, H. 2007, ApJ, 670, 928  
Bouwens, R. J., Illingworth, G. D., Oesch, P. A., et al. 2011, ApJ, 737, 90  
—. 2014, arXiv:1403.4295  
Bowler, R. A. A., Dunlop, J. S., McLure, R. J., et al. 2014a, arXiv:1411.2976  
Bowler, R. A. A., Dunlop, J. S., McLure, R. J., et al. 2014b, MNRAS, 440, 2810  
Bradley, L. D., Trenti, M., Oesch, P. A., et al. 2012, ApJ, 760, 108  
Bradley, L. D., Zitrin, A., Coe, D., et al. 2014, ApJ, 792, 76  
Bundy, K., Ellis, R. S., & Conselice, C. J. 2005, ApJ, 625, 621

- Cai, Z.-Y., Lapi, A., Bressan, A., et al. 2014, *ApJ*, 785, 65
- Cappellari, M., Bacon, R., Bureau, M., et al. 2006, *MNRAS*, 366, 1126
- Chae, K.-H. 2010, *MNRAS*, 402, 2031
- Charlot, S., & Fall, S. M. 2000, *ApJ*, 539, 718
- Choi, Y., Park, C., & Vogeley, M. S. 2007, *ApJ*, 658, 884
- Coe, D., Benítez, N., Sánchez, S. F., et al. 2006, *AJ*, 132, 926
- Coe, D., Bradley, L. D., & Zitrin, A. 2014, *arXiv:1405.0011*
- Coles, P., & Jones, B. 1991, *MNRAS*, 248, 1
- Collett, T. E., Marshall, P. J., Auger, M. W., et al. 2013, *MNRAS*, 432, 679
- Cooray, A. 2005, *MNRAS*, 364, 303
- Ellis, R., Santos, M. R., Kneib, J.-P., & Kuijken, K. 2001, *ApJ*, 560, L119
- Faber, S. M., & Jackson, R. E. 1976, *ApJ*, 204, 668
- Fassnacht, C. D., Moustakas, L. A., Casertano, S., et al. 2004, *ApJ*, 600, L155
- Finkelstein, S. L., Papovich, C., Dickinson, M., et al. 2013, *Nature*, 502, 524
- Finkelstein, S. L., Ryan Jr., R. E., Papovich, C., et al. 2014, *arXiv:1410.5439*
- Franx, M., Illingworth, G. D., Kelson, D. D., van Dokkum, P. G., & Tran, K.-V. 1997, *ApJ*, 486, L75
- Greene, Z. S., Suyu, S. H., Treu, T., et al. 2013, *ApJ*, 768, 39
- Grogin, N. A., Kocevski, D. D., Faber, S. M., et al. 2011, *apjs*, 197, 35
- Guo, Q., White, S., Boylan-Kolchin, M., et al. 2011, *MNRAS*, 413, 101
- Hathi, N. P., Mobasher, B., Capak, P., Wang, W.-h., & Ferguson, H. C. 2012, *ApJ*, 757, 43
- Henriques, B. M. B., White, S. D. M., Lemson, G., et al. 2012, *MNRAS*, 421, 2904
- Hilbert, S., Hartlap, J., White, S. D. M., & Schneider, P. 2009, *A&A*, 499, 31
- Hilbert, S., White, S. D. M., Hartlap, J., & Schneider, P. 2007, *MNRAS*, 382, 121
- Kelly, B. C., Fan, X., & Vestergaard, M. 2008, *ApJ*, 682, 874
- Kitzbichler, M. G., & White, S. D. M. 2007, *MNRAS*, 376, 2
- Koekemoer, A. M., Faber, S. M., Ferguson, H. C., et al. 2011, *ApJS*, 197, 36
- Kriek, M., van Dokkum, P. G., Franx, M., et al. 2006, *ApJ*, 649, L71
- Laureijs, R., Amiaux, J., Arduini, S., et al. 2011
- Madau, P. 1995, *ApJ*, 441, 18
- Maraston, C. 2005, *MNRAS*, 362, 799
- McCully, C., Keeton, C. R., Wong, K. C., & Zabludoff, a. I. 2014, *MNRAS*, 443, 3631
- McLure, R. J., Dunlop, J. S., Bowler, R. A. A., et al. 2013, *MNRAS*, 432, 2696
- Muñoz, J. A. 2012, *JCAP*, 2012, 015
- Muzzin, A., Marchesini, D., Stefanon, M., et al. 2013, *ApJ*, 777, 18
- Newman, A. B., Ellis, R. S., Treu, T., & Bundy, K. 2010, *ApJ*, 717, L103
- Oesch, P. A., Bouwens, R. J., Illingworth, G. D., et al. 2012, *ApJ*, 759, 135
- Ono, Y., Ouchi, M., Mobasher, B., et al. 2012, *ApJ*, 744, 83
- Parzen, E. 1962, *The Annals of Mathematical Statistics*, 33, 1065
- Pei, Y. C. 1995, *ApJ*, 440, 485
- Robertson, B. E., Furlanetto, S. R., Schneider, E., et al. 2013, *ApJ*, 768, 71
- Rosenblatt, M. 1956, *The Annals of Mathematical Statistics*, 27, 832
- Schechter, P. 1976, *ApJ*, 203, 297
- Schenker, M. A., Robertson, B. E., Ellis, R. S., et al. 2013, *ApJ*, 768, 196
- Schmidt, K. B., Treu, T., Trenti, M., et al. 2014a, *ApJ*, 786, 57
- Schmidt, K. B., Treu, T., Brammer, G. B., et al. 2014b, *ApJ*, 782, L36
- Schneider, P., Ehlers, J., & Falco, E. E. 1992, *Gravitational Lenses* (Springer)
- Schneider, P., Kochanek, C. S., & Wambsganss, J. 2006, *Gravitational Lensing: Strong, Weak and Micro* (Springer)
- Sheth, R. K., Bernardi, M., Schechter, P. L., et al. 2003, *ApJ*, 594, 225
- Somerville, R. S., Gilmore, R. C., Primack, J. R., & Domínguez, A. 2012, *MNRAS*, 423, 1992
- Spergel, D., Gehrels, N., Breckinridge, J., et al. 2013
- Springel, V., White, S. D. M., Jenkins, A., et al. 2005, *Nature*, 435, 629
- Suyu, S. H., Marshall, P. J., Auger, M. W., et al. 2010, *ApJ*, 711, 201
- Toft, S., Gallazzi, A., Zirm, A., et al. 2012, *ApJ*, 754, 3
- Trenti, M., & Stiavelli, M. 2008, *ApJ*, 676, 767
- Trenti, M., Bradley, L. D., Stiavelli, M., et al. 2011, *ApJ*, 727, L39
- . 2012, *ApJ*, 746, 55
- Treu, T. 2010, *ARA&A*, 48, 87
- Treu, T., Ellis, R. S., Liao, T. X., & van Dokkum, P. G. 2005, *ApJ*, 622, L5
- Turner, E. L., Ostriker, J. P., & Gott, J. R., I. 1984, *ApJ*, 284, 1
- Vale, a., & Ostriker, J. P. 2004, *MNRAS*, 353, 189
- van de Sande, J., Kriek, M., Franx, M., Bezanson, R., & van Dokkum, P. G. 2014, *ApJ*, 793, L31
- van de Sande, J., Kriek, M., Franx, M., et al. 2013, *ApJ*, 771, 85
- van der Burg, R. F. J., Hildebrandt, H., & Erben, T. 2010, *A&A*, 523, A74
- van der Wel, A., Holden, B. P., Zirm, A. W., et al. 2008, *ApJ*, 688, 48
- van Dokkum, P. G., Kriek, M., & Franx, M. 2009, *Nature*, 460, 717
- Windhorst, R. A., Cohen, S. H., Jansen, R. A., Conselice, C., & Yan, H. 2006, *NAR*, 50, 113
- Windhorst, R. A., Cohen, S. H., Hathi, N. P., et al. 2011, *ApJS*, 193, 27
- Wyithe, J., Yan, H., Windhorst, R. R., & Mao, S. 2011, *Nature*, 469, 181
- Wyithe, J. S. B., Turner, E. L., & Spergel, D. N. 2001, *ApJ*, 555, 504
- Yan, H., Yan, L., Zamojski, M. A., et al. 2011, *ApJ*, 728, L22
- Zitrin, A., Fabris, A., & Merten, J. 2014, *arXiv:1411.1414v1*